Design, Fabrication and Characterization of Ferromagnetic Artificial Bacterial Flagella

Master Thesis

Design, Fabrication and Characterization of Ferromagnetic Artificial Bacterial Flagella

Thomas F. Wuhrmann

Dr. Li Zhang and Dr. Salvador Pané i Vidal

Adviser

Prof. Dr. Bradley J. Nelson
Institute of Robotics and Intelligent Systems
Swiss Federal Institute of Technology Zurich (ETH)

2011-11

IRIS
Institute of Robotics and Intelligent Systems

ETH
Eidgenössische Technische Hochschule Zürich
Swiss Federal Institute of Technology Zurich

To my family

Preface

First of all I would like to convey my deepest gratefulness to my family. Especially I want to thank my parents who always believed in my decisions and final success, even in hard times. Also I would like to thank one more time my wife for her great support.

Furthermore I would like to express my sincere appreciation to my supervisors for their support and encouragement, Dr. Li Zhang who was every time open for a discussion how to advance the project and Dr. Salvador Pané i Vidal for his participation on complex processes and his effort in proper analysis.

Special thank goes to Prof. Dr. Bradley J. Nelson for his endorsement in my choice of the MSc in Micro and Nanosystems and for his good advices while looking for outstanding projects.

I would like to thank M. Arif Zeeshan for his technical assistance in imaging and all the analyses he performed for the project, Erdem C. Siringil for sharing his expertise on direct laser writing, Kathrin Peyer for all the help on manipulation of microrobots and Christian Peters for the collaborative work in setting up new processes. And for their effort in the magnetic property analysis a special thank goes to Prof. Dr. Jordi Sort Viñas and Dr. Eva Maria Pellicer Vilá from the Autonomous University of Barcelona.

Also I want to thank all people from the IRIS group for their time they spent on helping me to bring this project to success.

Finally, and especially after the diagnosis of carcinosis in my own family circle in recent years, I hope that I could have contributed to a successful treatment of cancer in future.

Zurich, $2^{nd} October 2011$
Thomas Wuhrmann

Abstract

Artificial bacterial flagellum (ABF), a helical microrobot, has potential to act as a biomedical robot for *in vivo* and *in vitro* applications such as targeted drug delivery, microsurgery, cell manipulation and single-cell analysis. In this work the design, fabrication and characterization of metallic ABFs are reported. Ferromagnetic structures, including CoNi, Fe and hybrid structures are obtained using 3-D laser lithography and electrochemical deposition. One advantage of the ferromagnetic ABFs is, compared to previously reported ABFs consisting of soft-magnetic heads and helical ribbon tails, larger magnetic torques can be generated for magnetic actuation due to a much larger volume of the magnetic material. Furthermore, ferromagnetic multi-segment ABFs can be obtained directly by successive electroplating. Ferromagnetic helical devices are promising for applications in highly viscous fluid environments, such as bio-fluids. Once functionalized, they have the potential to perform targeted delivery of energy (e.g., inductive heating) as well as chemical and biological substances.

The fabrication processes of ferromagnetic ABFs can be summarized by the following steps. First, a bare glass substrate is coated with an indium tin oxide (ITO) layer by e-beam evaporation. Then a positive tone photoresist (AZ9260) is spin-coated on the thermally treated ITO samples. Based on two-photon polymerization technique, 3-D lithographic patterning of hollow helical-shaped structures are performed using a direct laser writing tool provided by Nanoscribe GmbH. These substrates with vertical arrays of helical pores are then filled by electrochemical deposition with a CoNi alloy, Fe or multiple segments of different metals. Finally the freestanding ferromagnetic helical structures are obtained by removing the photoresist template.

The material properties of the metallic ABFs were investigated by SEM, EDX, FIB and VSM. Magnetic actuation tests were conducted in deionized water using a uniform rotating magnetic field. The results show that the metallic ABFs are capable of performing corkscrew motion and navigation in fluid.

In addition, two types of ferromagnetic ABFs are designed for bio-/chemical functionalization: (I) helical structures consisting of two or multiple segments of metals, such as Au and CoNi alloy; (II) encapsulation of ferromagnetic ABFs with carbon layers by a CVD process.

Zusammenfassung

Das 'Artificial bacterial flagellum' (ABF), ein spiralförmiger Mikroroboter, zeigt Potential für den Einsatz als biomedizinischer Roboter für *in vivo* und *in vitro* Anwendungen wie gezielte Medikamentenabgabe, Mikrochirurgie, Zellbehandlung sowie Zellanalyse. Diese Arbeit beschreibt das Design, die Fabrikation und die Charakterisierung von metallischen ABFs. Ferromagnetische Strukturen aus CoNi, Fe, sowie Hybride werden mittels 3-D Laser Lithographie und elektrochemischer Abscheidung hergestellt. Ein Vorteil von ferromagnetischen ABFs ist, verglichen mit bisher beschriebenen ABFs, dass durch ihr grösseres Volumen an magnetischem Material stärkere magnetische Drehmomente für den Antrieb generiert werden. Weiter können multi-segmentale ABFs durch sukzessive elektrochemische Abscheidung erzeugt werden. Ferromagnetische spiralförmige Objekte sind erfolgsversprechend für den Einsatz in hochviskösen Flüssigkeiten wie biologische Fluide. Örtliche induktive Erhitzung oder die Abgabe von chemischen und biologischen Substanzen (durch Funktionalisierung) sind möglich.

Der Fabrikationsprozess von ferromagnetischen ABFs kann mit den folgenden Schritten zusammengefasst werden: Zuerst wird ein Glas-Wafer mit Indium Zinn Oxid (ITO) mittels Elektronenstrahl-Verdampfung beschichtet. Das beschichtete Substrat wird nach Temperung mit positivem Fotolack (AZ9260) überzogen. Basierend auf der Zwei-Photonen Polymerisierungstechnik werden 3-D-laserlithographisch spiralförmige Hohlkörper strukturiert. Die vertikalen Poren werden anschliessend durch elektrochemische Abscheidung von CoNi Legierungen, Fe oder multiplen Segmenten verschiedenster Metalle aufgefüllt. Durch Auflösung des Fotolacks werden die Strukturen schlussendlich freigelegt.

Die Materialeigenschaften der metallischen ABFs wurden mittels SEM, EDX, FIB und VSM untersucht. Magnetantriebstests wurden in entionisiertem Wasser durchgeführt mittels gleichmässigen rotierenden Magnetfeldern. Die Resultate zeigten, dass die metallischen ABFs sowohl zur schraubenförmige Fortbewegung in der Lage sind als auch zur Navigation in Flüssigkeiten.

Zwei Designs von ferromagnetischen ABFs zur bio-/chemischen Funktionalisierbarkeit wurden verfolgt: (I) Spiralförmige Strukturen aus zwei oder mehreren metallischen Segmenten wie Au und CoNi Legierungen; (II) Durch einen CVD-Prozess mit Kohlstoffschichten überzogene ferromagnetische ABFs.

Contents

List of Tables

List of Figures

Notation

ABF	Artificial Bacterial Flagellum
ABFs	Artificial Bacterial Flagella
CP	'ConnectPoints' (gwl command)
ConnectPoints	[On,Off] gwl command for interpolation between points
EDX	energy dispersive X-ray spectroscopy
ESB	energy and angle selective backscattered electron detection
FIB	focused ion beam
gwl	general writing language (Nanoscribe script language)
ITO	indium tin oxide ($In_2O_3 : Sn$, typically 90% In_2O_3, 10% SnO_2)
PerfectShape	[On,Off] gwl command for automatic adjustments at edges
PPT	number of points per helix turn
SEM	scanning electron microscopy
stl	stereolithography CAD software file format
VSM	vibrating sample magnetometer

1   Introduction

Targeted drug delivery has been and still is one of the most important global research fields since decades. Next to other techniques like chemical attraction and guidance of nano containers, micro- and nanorobotic systems capable for biological functionalization provide most promising approaches in terms of controllability. Additional benefits of such robotic systems are possible applications in the field of microsurgery.

At the Institut of Robotics and Intelligent Systems (IRIS), which is part of the Swiss Federal Institute of Technology (ETH) in Zurich, microrobotics is one of the major research fields. Dr. Li Zhang *et al.*developed in 2009 untethered helical microswimmers, namely Arificial Bacterial Flagella (ABFs), similar in size an geometry to natural bacteria flagella (visible in Figure 1). Helical devices with
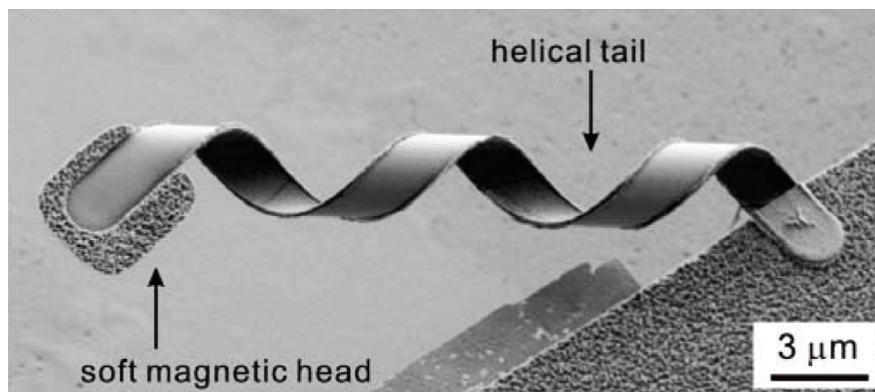
Figure 1: *Artificial Bacteria Flagellum (ABF) with a soft magnetic head and a helical tail ([19])*

non-magnetic tails and soft magnetic heads have been produced using MEMS fabrication technologies (see [18] for further details). These helical swimmers showed the capability to convert rotating magnetic fields to translational motion in a low Reynolds number regime ([19],[10]).

In 2011 the first helical microswimmers based on magnetic polymer composites have been developed (Figure 2). Studies on structures with magnetization along the whole microswimmer body were conducted and effects of different shapes observed. Although good results have been achieved the next logical step was the investigation of metallic helical structures.

Within the fabrication of diverse magnetic micro- and nanorobots, electrode-
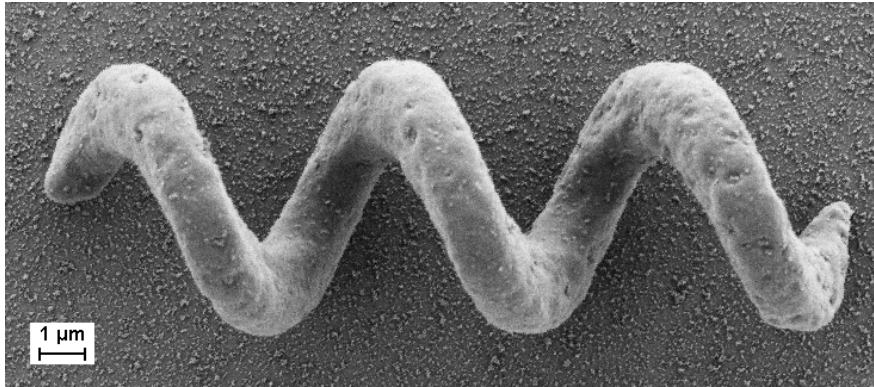
Figure 2: *Artificial Bacteria Flagellum (ABF) based on magnetic polymer composite ([13]).*

position is one of the major skills of the Institut of Robotics and Intelligent Systems. Inspired by an article published in Science in the year of 2009 ([4]), describing broadband circular polarizers made out of gold helix photonic meta-materials, the present project was finally initiated. Major goals were the exploration of a new microfabrication method and the combination of different ongoing projects of IRIS: On the one hand the development of the described ABFs and on the other hand the fabrication of micro- and nanowires capable for biological functionalization ([17], [16]). Artificial bacterial flagella (ABFs) have potential to act as biomedical robots for *in vivo* and *in vitro* applications. Microsurgery, cell manipulation and single-cell analysis are additional fields of application next to the already mentioned targeted drug delivery. Ferromagnetic ABFs could generate higher magnetic torques. Furthermore the possibility of wireless energy delivery based on inductive heating could provide medical applications such as hyperthermia.

1.1 Process Description

In this section the fabrication procedure is introduced. Figure 3 shows the required process steps from top to down. A documentation of all fabrication steps can be found in Chapter 3.

Conductive layer coating of a glass wafer: After a preliminary cleaning procedure of a bare glass substrate, a conductive layer was deposited. In this project Indium Tin Oxide (ITO) was used due to its high conductivity as
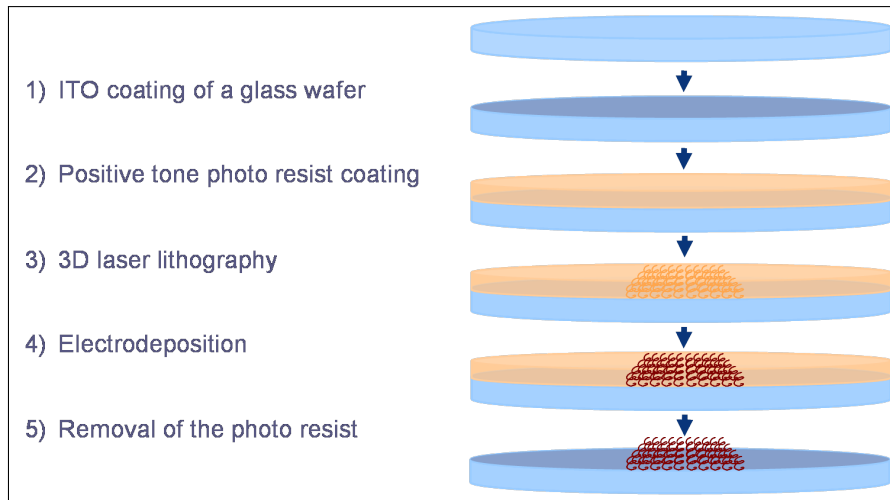
Figure 3: *The fabrication procedure: Beginning with a bare glass wafer (on the top) five steps are conducted to achieve complex shaped, free standing (metallic) structures.*

well as transparency in the visible range. This layer is required for the electrodeposition step.

Positive tone photoresist coating: For the lithographic step a positive tone photoresist was spincoated on the ITO coated samples. (Positive tone resists become more soluble by exposure of (UV-)light.)

3-D laser lithography: Direct laser writing was used to write complex shaped structures into the positive tone photoresist. In 3-D laser lithography the polymerization of the resist is initiated only in the regions where a high frequency laser beam is tightly focused for maximum intensity volumes (voxels). After exposure the structures need to be connected to the top of the resist layer for development and to achieve hollow structures.

Electrodeposition: The written structures need to have connection to the conductive layer underneath the resist as well. To fill up the complex shaped cavities electrolyte baths containing cobalt-nickel, iron and gold have been used. The deposition was conducted in direct current electroplating mode.

Removal of the photoresist: By removing the photoresist layer the structures were excavated for further analysis.

2 Materials and Methods

In the following sections the most important materials and methods used in this project are described. The order is according to the fabrication steps which is documented in Chapter 3.

2.1 Direct Laser Writing

The concept of direct laser writing (DLW), also known as 3D Laser Lithography, is based on two-photon absorption in photosensitive materials. In DLW systems a femtosecond laser provides high frequencies in order to polymerize the photoresist by the energy of two (or more) photons. This pulsed near-infrared laser is then tightly focused into a photoresist which is sensitive to near-ultraviolet radiation (see Figure 4). By exceeding the exposure threshold of the photoresist a volume
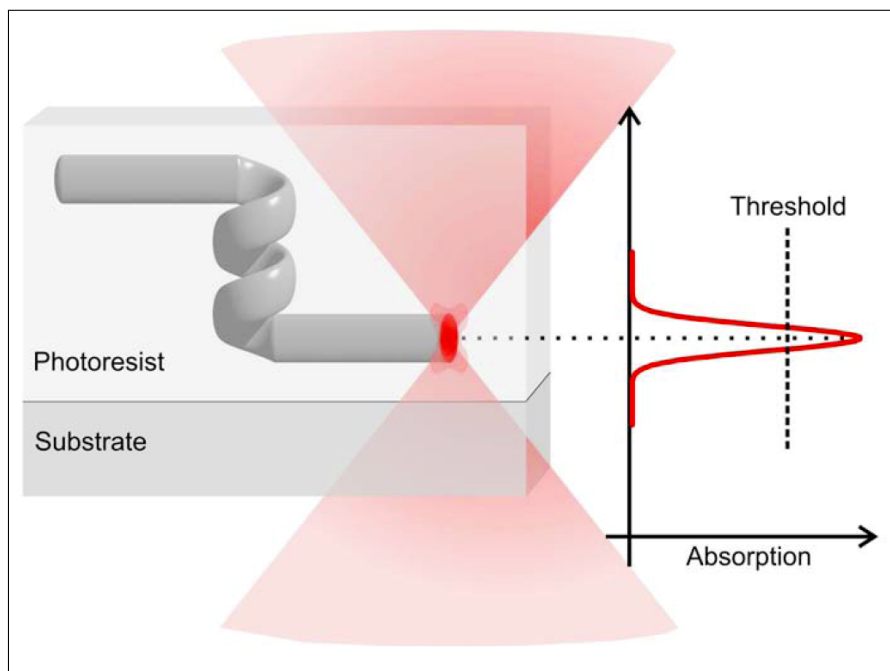
Figure 4: *Direct laser writing based on two photon polymerization: Only regions where the laser is tightly focused and the laser power is high enough are polymerized. Moving the sample relative to the focal volume enables writing of arbitrary trajectories.[15, Figure 4.1]*

pixel (voxel) is polymerized, and structures are written by scanning the sample along arbitrary trajectories relative to the focal point. The shape of the voxel

is ellipsoidal, with an aspect ratio of about 2.7. It is determined by several parameters, e.g., the laser mode, the numerical aperture (NA) of the objective and the refractive-index mismatch between the resist and the immersion system. The resolution of a conventional optical imaging system is defined by the diffraction limit. The minimum lateral ($\Delta r_\parallel$) and axial ($\Delta r_\perp$) distance between two point-spread functions distance is given by

$$\Delta r_\parallel = 0.6098 \frac{\lambda}{NA} \tag{2.1}$$

and

$$\Delta r_\perp = 2 \frac{n\lambda}{NA^2} \tag{2.2}$$

where λ is the wave length of the light source, n the refracitve index of the polymer and NA the numerical aperture of the imaging system. By assuming a wavelength of 780nm, NA=1.4 and a refractive index of 1.518 the Δr is laterally limited to 340 nm and axially to 1208 nm. Besides the defraction limit there are factors, like laser stability, proximity effects and mechanical properties of the features, which influence the achievable resolution of the system. [15]

2.1.1 Positive Tone Photoresist AZ9260

In this project the photoresist AZ9260 was used, provided by MicroChemicals GmbH in Germany. This positive tone photoresist is recommended for galvanization[1]. The photoreaction which occurs during the exposure is visualized in Figure 5. The chemical reaction is based on DNQ-sulfonate inhibitors bounded on the polymer. During the exposure the DNQ-sulfonate is converted into indene carboxylic acid. Compared to the unexposed inhibitor the carboxylic acid yields to orders of magnitude higher resist development rates.[1, Exposure of Photoresists]

During the project the AZ826MIF developer[2], also provided by MicroChemicals GmbH, was used to set up the process. Although there might be other developers which provide better resolutions, it is a ready-to-use developer which is commonly used for new processes. It has to be mentioned that this developer

---

[1]Different tested resists are well summarized in [15, Table 4.1]

[2]Important remarks on process optimization in terms of the choice of the developer are mentioned in Section 6
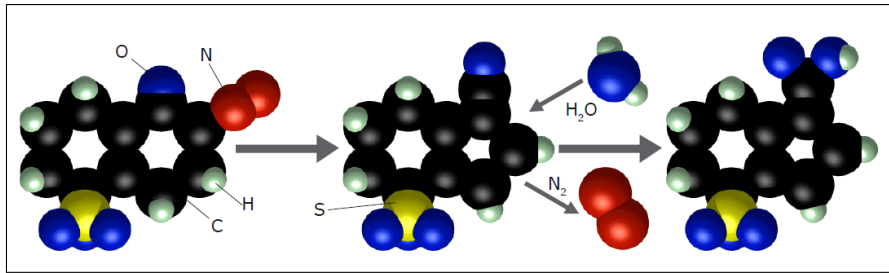
Figure 5: *Photoreaction in DNQ based positive tone photoresists: By exposure with matched UV-light the photo active compound DiazoNaphtoQuinone-(DNQ-)sulfonate (the inhibitor) is converted into indene carboxylic acid (by replacing a nitrogen with a water molecule).[1, Exposure of Photoresists]*

contains special additives which allows scum free developing. However the additives also cause increased dark erosion (see [1, Resists, Developers and Removers] for further information).

2.1.2   Nanoscribe Photonic Professional Setup

The Nanoscribe Photonic Professional system, a direct laser writing system provided by Nanoscribe GmbH in Germany, is shown in Figure 6[3]. Next to the
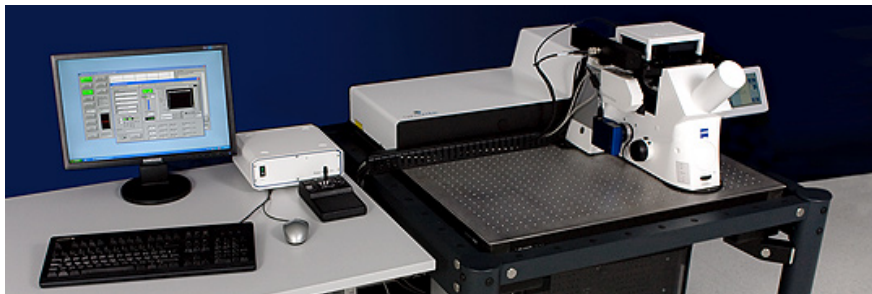
Figure 6: *Nanoscribe Photonic Professional system: On the optical table an inverse microscope (right side) and the laser and optics cabinet (behind the microscope) is visible (the electronics rack is located underneath the optical table).*

laser and optics cabinet and the electronics rack, an inverse microscope is installed. This microscope, an Axio Observer.Zi from Carl Zeiss MicroImaging GmbH, was equipped with three objectives, two air objectives with 50x and 63x magnifications ($NA \leq 1$) and an oil immersion with 100x magnification (NA

---

[3]http://www.nanoscribe.de/data/image/dlw-system3.jpg 08.09.2011

1.4). For highest resolutions the oil immersion objective was used for the fabrication described in this work. The motorized stage mounted on the microscope served for fast scanning purposes like changing the writing location on a sample. For high resolution writing only the piezoelectric stage (mounted on the motorized stage) was used which allows to navigate the structures in a volume of $300\,\mu$mx$300\,\mu$mx$300\,\mu$m.

2.2   Electrochemical Deposition

Electrochemical deposition is a common fabrication method to produce metallic layers on a conducting surface. To start the process, a constant current or voltage in between the working electrode (namely the sample itself) and a counter electrode is set while the electrodes are immersed in an electrolyte bath. Negative charges are delivered onto the conductive target area and positively charged metallic ions from the metal salt solution are attracted. When the ions reach the negatively charged surface, electrons are provided to reduce the positively charged ions to their non-charged, metallic form.

2.2.1   Electrolyte Bath: Cobalt-Nickel, Iron and Gold

Three different metals, respectively metal alloys, have been deposited within this project. The composition of the electrolyte baths is listed in the Table 1 to 3. Table 4 summarizes the recommended operating conditions for each electrolyte bath.

Table 1: Cobalt-Nickel electrolyte bath composition

Components	Amount	Function
Nickel Sulfate 6 H_2O	300 g/L	Main nickel source
Nickel Chloride 6 H_2O	30 g/L	Secondary nickel source
		Chlorides improves conductivity
		of bath, prevent passivation /
		improves corrosion of the anode
Cobalt Sulfate 6 H_2O	40 g/L	Main cobalt source
Boric Acid	20 g/L	pH buffer in cathode film, prevent
		precipitation and deposition of
		nickel hydroxide, helps to establish
		upper limits of current density
Citric Acid anh.	40 g/L	Complexing agent
Saccharin	2 g/L	Grain refiner
Tergitol-08	50 g/L	Surfactant, decreases pitting due
		to hydrogen evolution by decreasing
		the surface tension

Table 2: Iron electrolyte bath composition

Components	Amount	Function
Iron (II) Sulphate	0.2 M	Main iron source
Glycine	0.1 M	pH buffer in cathode film and bath stabilizer
Ascorbic Acid	0.5 g/L	Bath stabilizer

Table 3: Gold electrolyte bath composition

Components	Amount	Function
Gold Potassium Cyanide (66%)	8 g/L	Main gold source
Potassium Citrate	90 g/L	pH buffer
Citric Acid	90 g/L	Complexing agent
Brightener Concentrate	10 mL/L	Grain refiner

Table 4: Operating conditions for the Cobalt-Nickel, Iron and Gold electrolyte bath

Parameters	Cobalt–Nickel	Iron	Gold
Current density (j)	$-50\,\frac{\mathrm{mA}}{\mathrm{cm}^2}$	$-150\,\frac{\mathrm{mA}}{\mathrm{cm}^2}$	$-10\,\frac{\mathrm{mA}}{\mathrm{cm}^2}$
Anode material	Nickel	Platin. Titanium	Platin. Titanium
Temperature	$55\,°\mathrm{C}$	$25\,°\mathrm{C}$	$35\,°\mathrm{C}$
Magnetic stirring	200 rpm	200 rpm	none
Bubbling agitation	nitrogen, smooth	nitrogen, smooth	air
pH	5 to 7	4 (preparation pH)	4

2.2.2   Conductive Layer: Indium Tin Oxide (ITO)

Indium tin oxide (ITO) is used for several industrial applications like display fabrication, solar cells and a wide range of optical coatings. The heavily-doped n-type semiconductor ($In_2O_3 : Sn$, typically 90% In_2O_3 and 10% SnO_2 by weight) with large bandgap of around 3.5 eV (350 nm) provides good conductivity and high optical transparency in the visible range.[5][7]. As the laser beam of the Nanoscribe setup needs to pass the substrate and the conducitve layer the mentioned properties matched for direct laser writing as well as for electrodeposition. The deposition of the ITO layers have been conducted on a Univex500 e-beam evaporator.

2.2.3   DC Mode Plating Setup

For all metals which have been plated, DC-Plating in constant current-mode was conducted using an Autolab PGSTAT302N provided by ECO CHEMIE BV with Nova 1.7 software installed. With this system it is possible to apply currents in the region of milli amperes in a controlled fashion while measuring the voltage response of the system. There was no reference electrode in use. To assure continuous agitation a magnetic stirrer system as well as smooth nitrogen (for CoNi and Fe) or air (for Au) bubbling was installed. The bubbling additionally helps to avoid hydrogen bubble formation on the plating surface.[4].

---

[4]Hydrogen evolution reaction: Hydrogen gas is generated at the cathode by the reduction of water molecules on an aqueous solution [2, Dictionary]

2.3   Magnetic Actuation Setup

Figure 7 shows the manipulation setup for rotational magnetic field testing. Three
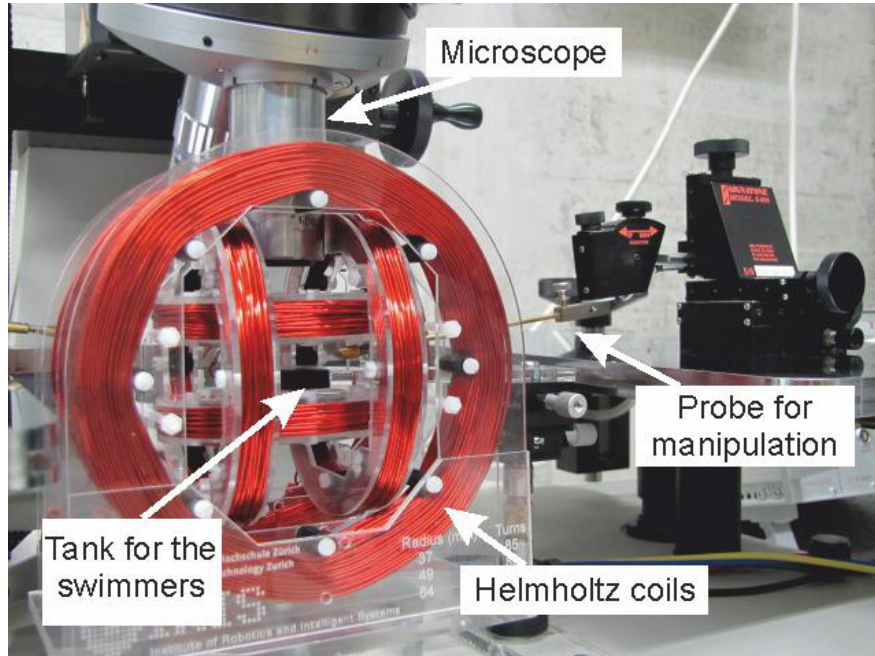
Figure 7: *Three Helmholtz coil setup for rotational magnetic field testing.[13]*

Helmholtz coils placed orthogonally to each other generate a uniform rotating magnetic field in the center of the system. The field direction can be rotated by varying the currents applied to the coils. A detailed description of this system can be found in [20]. The artificial bacteria flagella were placed in a tank with deionized water which was then positioned in the center of the coils. The microstructures have been mechanically detached from the substrate by using a probe. For observations the coil setup was positioned underneath an optical microscope equipped with a CCD camera.[13]

3   Fabrication

The first part of this chapter describes the processes to achieve templates for electrodeposition using 3-D laser lithography. The last two sections are pointing out several important parameters concerning the deposition of cobalt-nickel (CoNi), iron (Fe) and gold (Au) using the prepared templates as well as the liberation of the structures.

3.1   Substrate Preparation

Commercially available circular microscope coverslips with a diameter of $30\,\mathrm{mm}$ and a thickness of #1 $(0.13 - 0.16\,\mathrm{mm})$[5] served as substrates. For the preparation of subsequent processes a standard cleaning process has been conducted. It is recommended to use the special holders provided by Nanoscribe GmbH for the cleaning steps in liquids as the wafers tend to stick due to surface tension.

While using sonication the glass wafers have been washed in acetone and isopropanol for ten minutes each. Then the wafers were rinsed in deionized water and blown with nitrogen gas. To completely dry the glass substrates they have been heated for ten minutes on a hotplate set to $110\,^{\circ}\mathrm{C}$.

3.1.1   E-Beam Evaporation of Indium Tin Oxide (ITO)

To apply the conductive layer required for electrodeposition, indium tin oxide (ITO) has been evaporated on the cleaned substrates. The chamber pressure was pumped down to $10^{-6}\,\mathrm{mbar}$ or below before depositing the ITO with a thickness of $25\,\mathrm{nm}$. The e-beam was driven by a voltage of $10\,\mathrm{kV}$ and a current of around $11 - 14\,\mathrm{mA}$ was applied to evaporate the material. The deposition rate was around $1.4 - 1.6\,\mathrm{\AA/s}$. The deposited ITO layer showed already a certain conductivity although it was amorphous and therefore not as transparent and conductive as desired. To achieve a better transparency and less resistance an annealing of $260\,^{\circ}\mathrm{C}$ for three minutes in air on a hotplate was subsequently conducted for all coated substrates.[6]. It has to be pointed out that the samples should be placed slowly and carefully on the hotplate (too fast handling will cause breaking of the substrate due to thermal shock) or an oven could be used as an alternative

---

[5]http://www.menzel.de/Deckglaeser.675.0.html?id=675L=1 17.08.2011
[6]A temperature of 250 $^{\circ}\mathrm{C}$ is recommended for crystalline, water-free ITO films [7]

approach. Due to the thermal treatment the ITO becomes recrystallized and the film gains in transparency. Additionally the sheet conductance is improved by a factor of approximately 20 which is mainly caused by an uptake of oxygen.[7] The

(a) 22 °C	(b) 150 °C	(c) 200 °C	(d) 250 °C	(e) 300 °C
35 kΩ	30 kΩ	20 kΩ	1 kΩ	1 kΩ
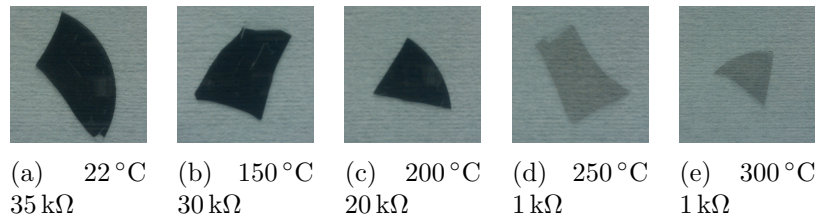
Figure 8: *Thermal treatment of ITO and qualitatively measured resistances (two-point measurements with ten millimetres probe distance).*

sheet resistance[8] of the ITO coated substrates prepared as described above and used for further processing reached $2.5 \pm 0.5 \, \text{k}\Omega/\text{cm}^2$.

Figure 8 shows the results of a test run for different annealing temperatures. Annealing in nitrogen enriched environments did not show any significant changes on conductivity or transparency.

3.1.2   Spincoating of AZ9260

Samples for electroplating need a contact area for the electrical clamp. Two possible methods have been discussed to provide such an area: (I) Use of a lift-off tape or (II) photo lithographic removal of the resist. Although the second option would provide a cleaner and less destructive removal, the lift-off tape was chosen for faster processing. Figure 9(a) shows an ITO coated wafer with attached lift off tape prepared for spincoating. Once the tape is placed on the wafer, the positive tone photoresist AZ9260 has been applied by spincoating. The recipes which have been followed to coat the ITO substrates can be found in Appendix A. In Figure 9(b) a spincoated wafer is visible after the removal of the lift off tape.

---

[7]Another way of depositing ITO is described in [7] or [6]: ITO sputtering in oxygen rich environments leads to electrical isolating but transparent layers where a subsequent annealing step at 460 °C is performed to gain in conductivity again.

[8]Four-point probe measurements, refer to [14] for further details

(a)   (b)
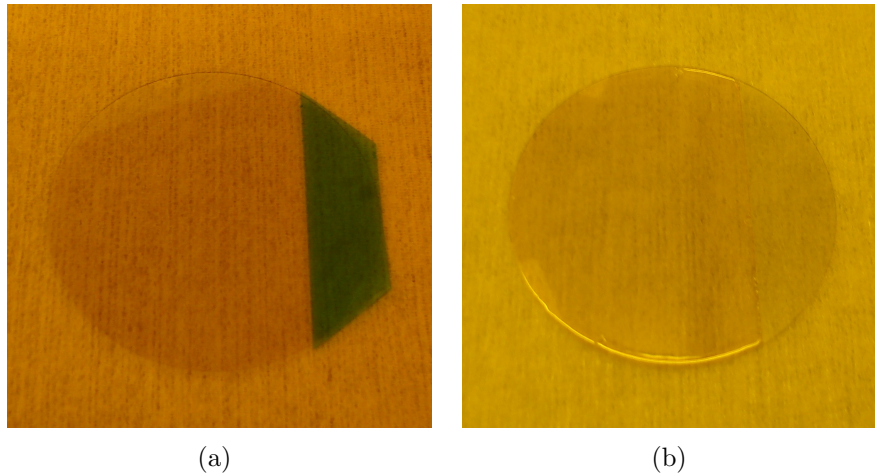
Figure 9: *Positioning of a lift off tape on an ITO coated substrate (a) and wafer after spincoating and lift off (b).*

3.2 3-D Laser Writing

Depending on the structures size, there are different ways of programming. Structure dimensions which are close to the resolution of the optics and the photoresist (around one micrometer in the present work) are written in single lines. Increasing the linewidth can be done by writing multiple lines next to each other. For solid structures with side lengths of more than five micrometers it can become easier to use the slicing software tool.

3.2.1 Programming of Solid Structures

Solid structure writing was used for labelling the written patterns during writing parameter tests. Additionally structures with a well known area of contact to the ITO layer have been written. In these cases the labels were drawn in the CAD software NX 7.5. By exporting the solids into an stl-file, they become readable for the slicing tool. For the positive tone photoresist the slicing has been done twice: First the slicing in X or Y direction generates the laser writing paths resulting in columns. The second slicing is conducted in Z direction to achieve a contour file which is also using columns. The generation of columns instead of woodpile like structures is recommended due to developing from the surface.

3.2.2   Programming of Single Line Structures

The programming of single lines structures have been done in Mathworks MAT-LAB R2010b. Helical and other structures have been defined using the codes provided in Appendix B. The functions included in this codes allows the adjustment of the number of turns, the pitch and the radius of the helix and finally the points per turn (PPT) as well as offset coordinates in x and y directions. The output of the function generates a three columns vector (m x 3) containing the coordinates of the path the laser is following. The main m-file (MATLAB code with included functions) served to generate arrays of structures. Additionally this code contains the sequence to store the predefined path (vector) in a gwl-file (the file format used by Nanoscribe).

3.2.3   Writing structures

The gwl-files prepared as described in Section 3.2.2 and / or 3.2.1 contain the paths to be followed by the laser. Writing parameters like scan speed, laser power and different writing modes need to be defined before the structure files are included. Examples of gwl-codes can be found in Appendix B. Furthermore, explanations are given on how to include additional features for fully automatized writing of more than one sample in one run.

To assure that the structures reach the bottom as well as the top of the resist layer, the design should overlap a few micrometers in both directions. Figure 10 shows an example how the interface was set to achieve that the structure was partly written into the glass substrate (anchoring) and into air. While using photoresist thicknesses underneath 15 μm (achievable by single layer coating) the 'interphaseposition' was set to as follows:

$$Interphaseposition =' photoresist\ thickness' +' glass\ anchoring\ height' \quad (3.1)$$

Due to the thin layer of photoresist the interface 'glass-photoresist' is not recognizable for Nanoscribe and the interface 'photoresist-air' will be found as this one is much stronger in terms of different refractive indices. For thicker layers of resist, namely more than 15 μm (achievable by double layer coating) the inter 'glass-photoresist' starts to be recognizable. It is still the weaker interface and it is recommended to use positioning according to Equation 3.1 up to 20 μm to
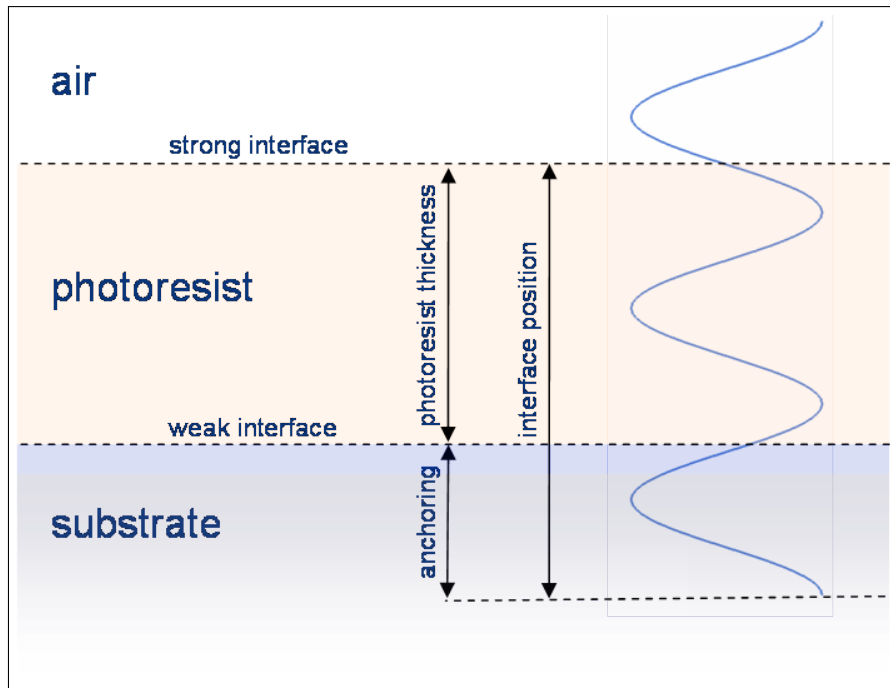
Figure 10: *Structure positioning relative to the interfaces of air-photoresist and photoresist-substrate.*

avoid a loss of interface during writing (due to uniformities). Figure 11 showes a print screen from the autofocus parameters for interface recognition using a photoresist thickness of ten micrometers. The weaker interface (B) is completely overlaid by the stronger interface (A). By increasing the 'minimal amplitude' (C) up to the value of 250 it is assured that the stronger interface will be found. In terms of sample writing times it would generally be desirable to use the 'glass-photoresist' interface as there, having a much flatter surface of the glass, is only one tilt correction measurement necessary (local tilt corrections are recommended for every 300x300 µm array when using the 'photoresist-air' interface).

3.3   Development of Structures

As already mentioned in Section 2.1.1 the developer AZ826MIF has been used in this work. Dependent on the thickness of the resist and the complexity of the structures to be developed the development time need to be adjusted. One minute of development per micrometer resist thickness plus 2.5 min additional
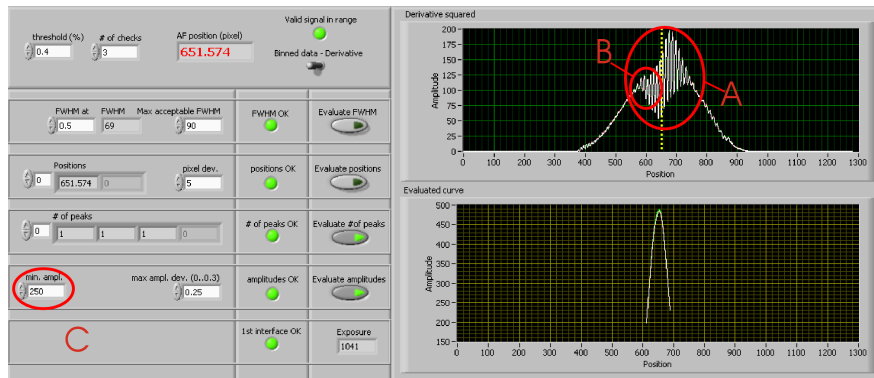
Figure 11: *Nanoscribe user interface print screen of the autofocus parameters for interface recognition. Highlighted: Position of the strong (A) and the weak (B) interface signals, setting for the 'minimal amplitude' (C)*

development time was used.[9] The development has been conducted with sonication. A subsequent rinsing step in deionized water and sonication was followed by nitrogen blow dry.

3.4 Electrodeposition

Before starting the electrodeposition the structured samples have been taped along the borders and around the structures itself. Such a prepared sample is shown Figure 12(a). By covering regions where ITO might be uncovered (borders or scratches and bubbles in photoresist) the risk of tunnelled plating beside the structures can be minimized. As a next step the electrical clamp has been attached and covered with Teflon tape (Figure 12(b) to avoid plating directly on the ITO or even on the clamp. Processes including the settings for Nova can be found in Appendix

3.5 Removal of the Photoresist

After the electrodeposition the sample have been cut with a diamond cutter from the backside to get rid of the taped parts. To liberate the structures, the photoresist was removed by immersing the samples in acetone for 10 minutes. For cobalt-nickel and gold structures a subsequent rinsing (approximately one minute each) in isopropanol and deionized water and finally drying the samples

---

[9]The experimental determination for the development times is described in Section 4.2.

| (a) | (b) |
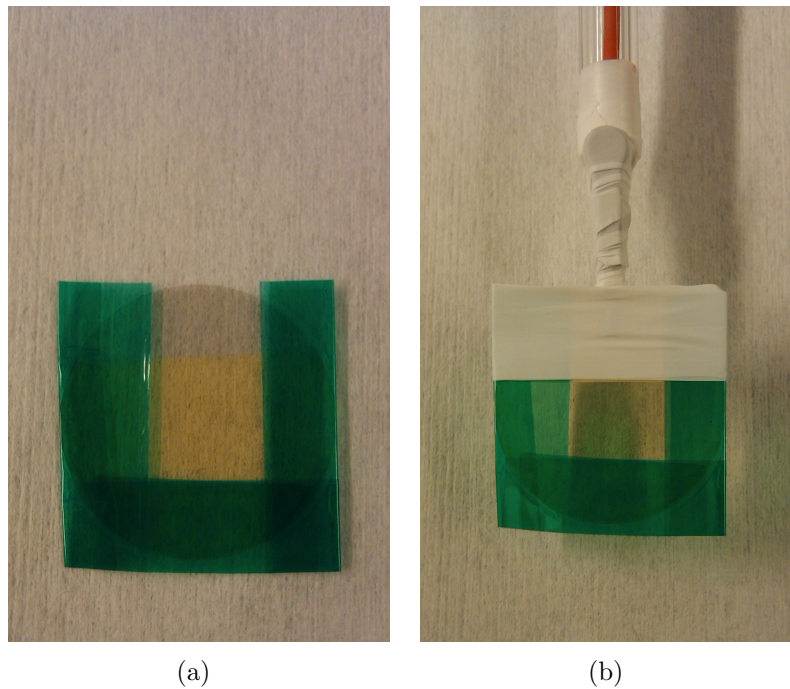
Figure 12: *Taped sample for covering possible regions of uncovered ITO (a) and teflon taped sample with attached clamp (b).*

on a hotplate set to 110 °C was conducted. Iron samples have been immersed in ethanol after the rinsing in acetone and let dry out by themselves to avoid oxidization of the structures.

3.6   Conclusions

The ITO layers deposition described in Section 3.1.1 was not completely optimized for highest transparency and conductivity. Evaporation in oxygen rich environments (compare [7] or [6] and annealing temperatures up to 500 °C could improve the mentioned properties further more. With a higher transparency experimental test runs on bare glass wafers would show closer 3-D lithographic results to those on ITO coated substrates. A gain in conductivity could help to improve electrodeposition results. Uniform coverage could already be achieved while applying lower current densities.

Due to the delicate handling of the thin glass substrates the overall fabrication yield of intact samples was around 60%. Regarding the fact that cracked or even broken samples can sometimes be used, it could be raised to about 75%. Most

of the samples initially started cracking during the clamp attachment in the ITO coating step. These cracks caused later the destruction of the samples while removing the lift-off tape.

4   Experimental Parameter Identification

This chapter describes some concepts to derive parameters for direct laser writing, development and electrodeposition. Whenever changing a process step, it is recommended to repeat at least some of these procedures to achieve optimized results.

4.1   Determination of Writing Parameters

Before starting the electrodeposition a few tests to determine the best writing modes, scan speed and laser power for solid or single line structures have been conducted. The goals of these tests conducted on bare glass substrates coated with photoresist were practicing, testing of new programs and finally speeding up the writing.

The first test patterns written were three layers of lines with incrementally increasing spacing (Figure 13(a) and (b) left). This pattern was written to determine the minimal distance for the separation of proximate lines. It can be

(a) Line spacing test pattern 1: CAD drawing

(b) Line spacing test pattern 1 and helices: Light microscopy image
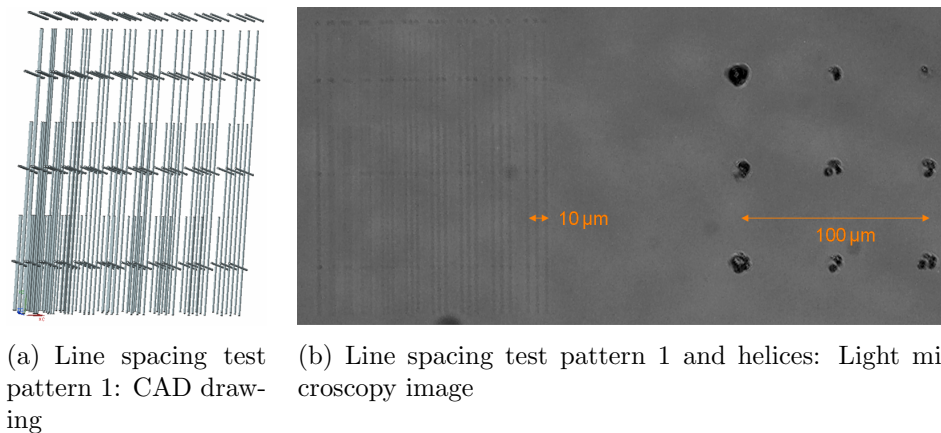
Figure 13:   *CAD drawing of the line spacing test pattern (a) and a light microscopy image of the pattern and helices written with same writing parameters (b).*

seen that the lines are separated when a distance of around 2.5 μm is granted for the used writing parameters (PerfectShape On, ConnectPoints On, ScanSpeed 200 and LaserPower 20). No visible effects from overlaying lines could be found. This qualitive result lead to the decision to keep a spacing and therefore a pitch

of more than 2.5 μm. Furthermore the first helices have been written on the
same sample (Figure 13(b) right) using the same writing parameters. The helical
structures have been burned while the lines from the test pattern have not.

The second test pattern contained single line columns, limited by two (as
reference) or multiple points, and helix arrays. All of them with different number
of points per turn (PPT)[10] and conditions with ConnectPoints ON (CP ON)
and ConnectPoints OFF (CP OFF) (see Figure 14). Increasing PPT resulted in
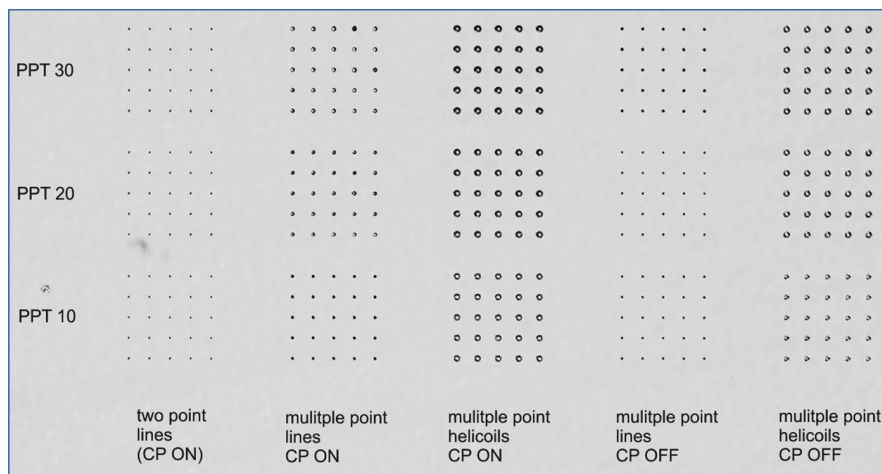
Figure 14: *Light microcopy image: Columns and lines arrays with different
number of points per turn and point interpolation (ConnectPoints) mode on and
off (PefectShape On, LaserPower 20, ScanSpeed 150)*

increasing filament diameter but the effect was nearly negligible when CP was
turn ON. With CP OFF a clear lost of helix shape was visible in between PPT 10
and PPT 20 arrays. When ConnectPoints mode is turned ON, Pointdistance or
UpdateRate need to be set for reproducible settings of the scan speed (for CP ON:
*ScanSpeed = UpdateRate * Pointdistance*, for CP OFF: *ScanSpeed = UpdateRate
* PPT*). For reproducible scan speed settings the Pointdistance has been set to
50 μm while ConnectPoints was set ON for all further writing procedures. This
allowed changes in the helix structure programming independently of the distance
of written path points.

---

[10]See 3.2.2 for further details
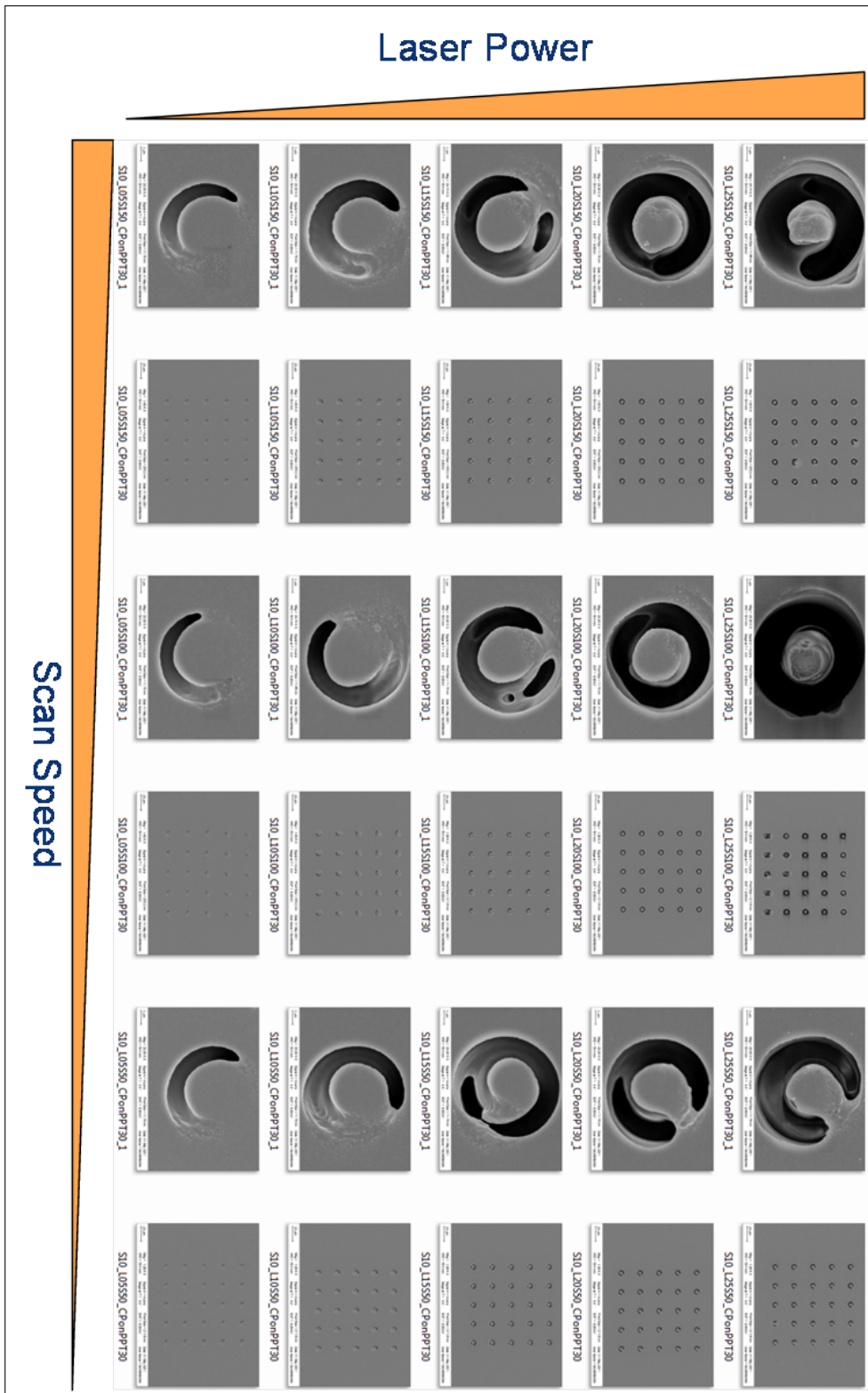
Figure 15: *SEM top view images of helices: Laser power vs. scan speed written in PerfectShape ON mode (PPT 30, CP On, AZ826MIF* 5 min*)*

Test pattern two has been written with different laser power and scan speed to analyze further conditions. The focus for the further comparisons as visible in Figure 15 have been set to helices with PPT 30 and CP ON as they have shown the best results in the previous comparison. Furthermore there was no observable increase in writing speed when PPT was reduced. Increasing the laser power results in stronger and wider filaments of the structures. Laser power of 15% (middle row) and more resulted in interconnected filament turns, laser power 25% even burned the sample. Decreasing the scan speed did not show any influence on the filament diameter or shape, although there should be less intensity applied within the same time. The effective scan speed was much slower than the set value and did not change significantly in between different scan speeds. It needs to be pointed out that the PerfectShape mode was turned on within this sample, which is believed to be the reason for the unexpected results concerning scan speed.

<div align="center">

(a) PerfectShape On   (b) PerfectShape Off

</div>
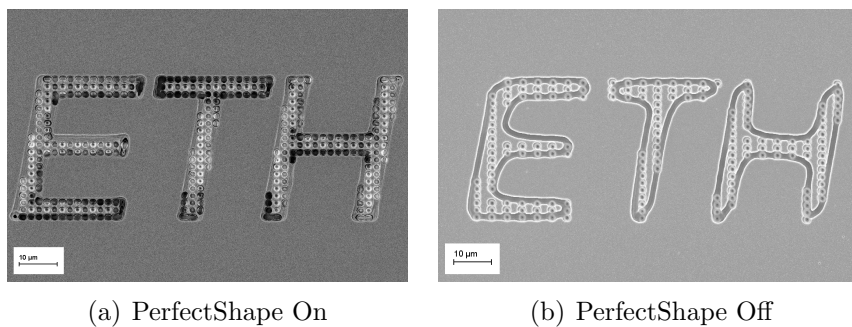
Figure 16: *SEM images of ETH logos: Written in PefectShape ON (a) and PerfectShape Off mode (b) (LaserPower 20, ScanSpeed 200, ConnectPoints ON, AZ826MIF 5 min*

The effects of the PerfectShape mode is visualized in Figure 16. It can be seen that in Figure 16(a) the capitals are written with sharp edges and straight lines while in Figure 16(b) the contour roundish. Using the PerfectShape feature grants the writing of structures exactly on their programmed coordinates. The laser is automatically slowing down and reducing laser power whenever the coordinates change from a straight line. For a complex 3-D structure like a helix, where there are no straight lines at all, the laser is constantly hold at a certain speed predefined by PerfectShape mode. In other words, the feature is permanently recognizing corners during the writing process.
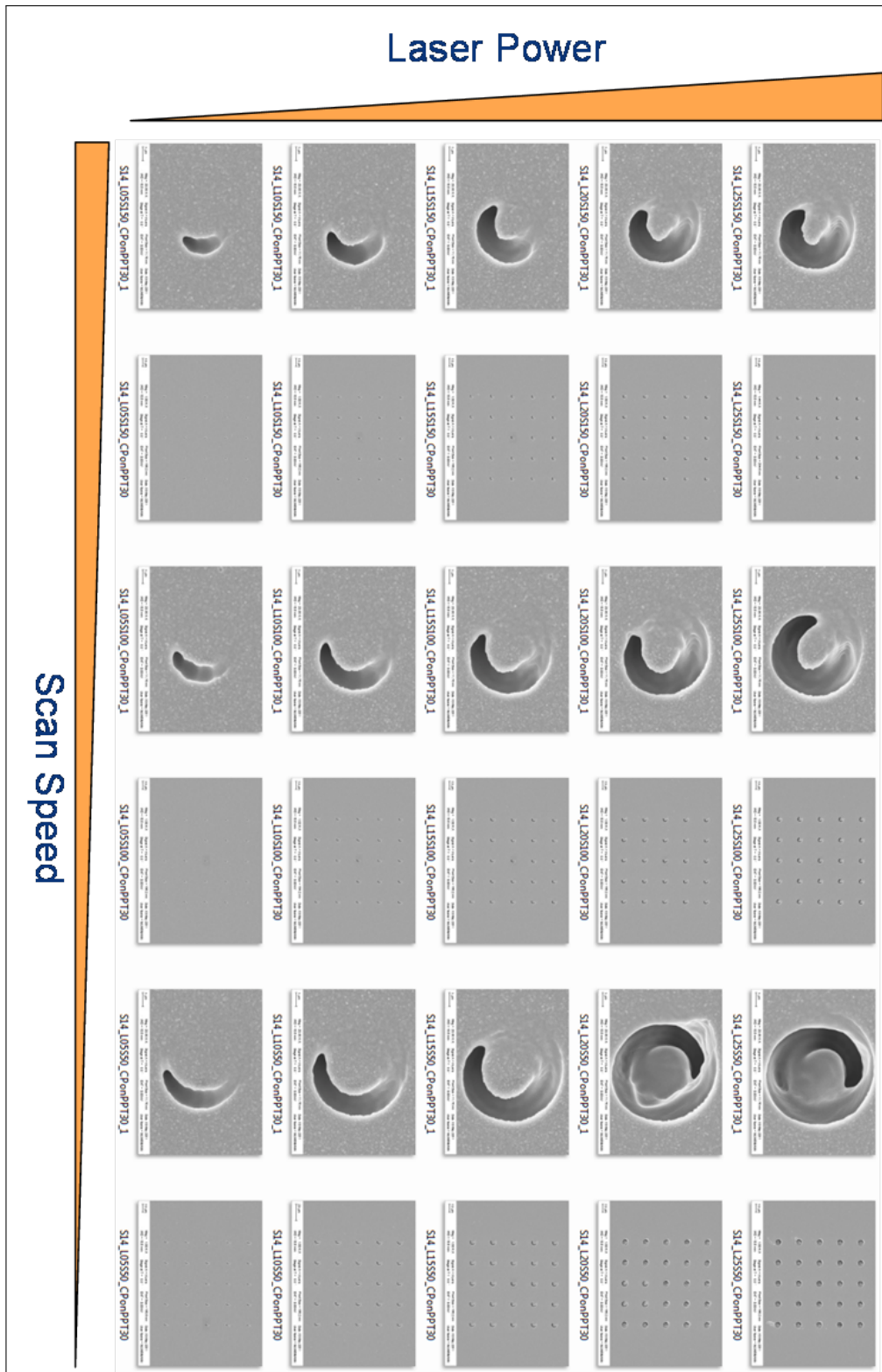
Figure 17: *SEM top view images of helices: Laser power vs. scan speed written in PerfectShape OFF mode (PPT 30, CP On, AZ826MIF* 5 min)

Figure 17 presents the comparison of laser power and scan speed with PerfectShape turned OFF. An increase of the writing speed resulted this time as expected in weaker filaments but the diameter of the helices was also reduced with higher scan speed.

4.2   Determination of Development Time

Some test runs to determine the time for development of the structures have been conducted. For a sufficient developing time the structures would reach the conductive layer (ITO) while effects of grey erosion are kept on a minimum. Figure 18 and Figure 19 shows series of different development times. For better comparison the helices have been written either upwards ('up' - from substrate to air) or downwards ('down' - from air to substrate). Longer development is leading to an increased etching of the structures at the resist-air (respectively resist-developer) interface due to a certain rate of dark erosion[11]. Furthermore a difference between up and downwards written structures becomes visible for increased developing times. In this stage of the project the coating of ITO had just been started and the effects of annealing have not been investigated then. The increased transparency of the amorphous ITO layer leads to the result that structures written with the lowest laser power (5%) are insufficiently polymerized and therefore not properly developed. This investigation indicates that the structures in Figure 17 written with lowest laser power (5%) were already close to the limit before the polymerization would not be initiated any more. To prove the samples for full development, some of the structures have been cut by focused ion beam (FIB). Figure 20 shows the conditions of 7.5 min (a) and 12.5 min (b) written with 20% (a) and 25% (b) laser power in downwards direction.

It is visible in Figure 20(a) that insufficient development results in not even one full helix turn, while Figure 20(b) is showing a fully developed structure with a cavity reaching the substrate. As an artefact of cutting hollow structures the appearance of the shown cavities is partly non-uniform.[12]

---

[11]see Section 2.1.1 for further details

[12]FIB cuts of metal filled structures as visible in Figure 23) showed results of better uniformity.
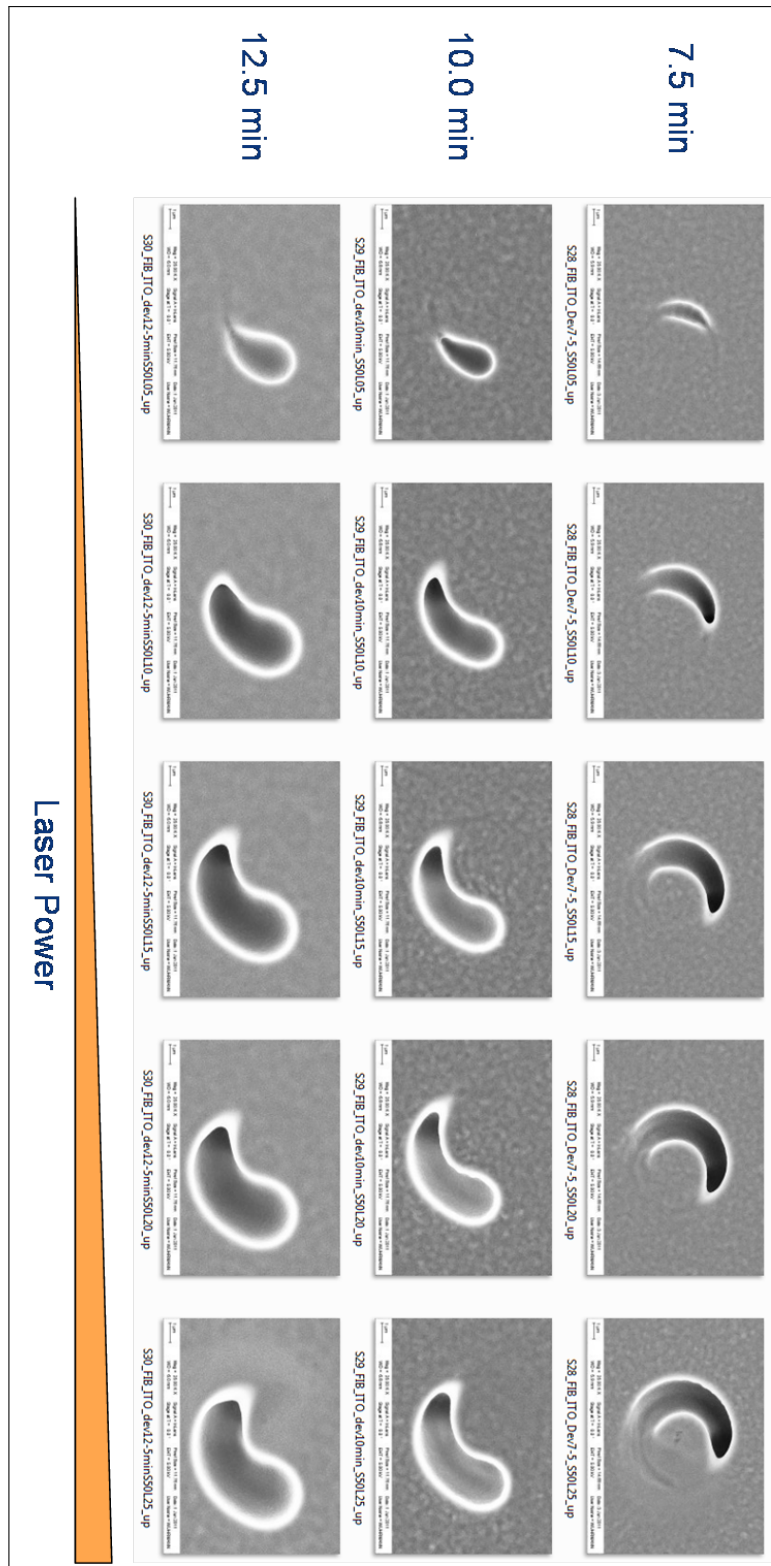
Figure 18: *SEM top view images of helices written in upwards direction, developed in AZ826MIF for* 7.5 min, 10 min *and* 12.5 min.
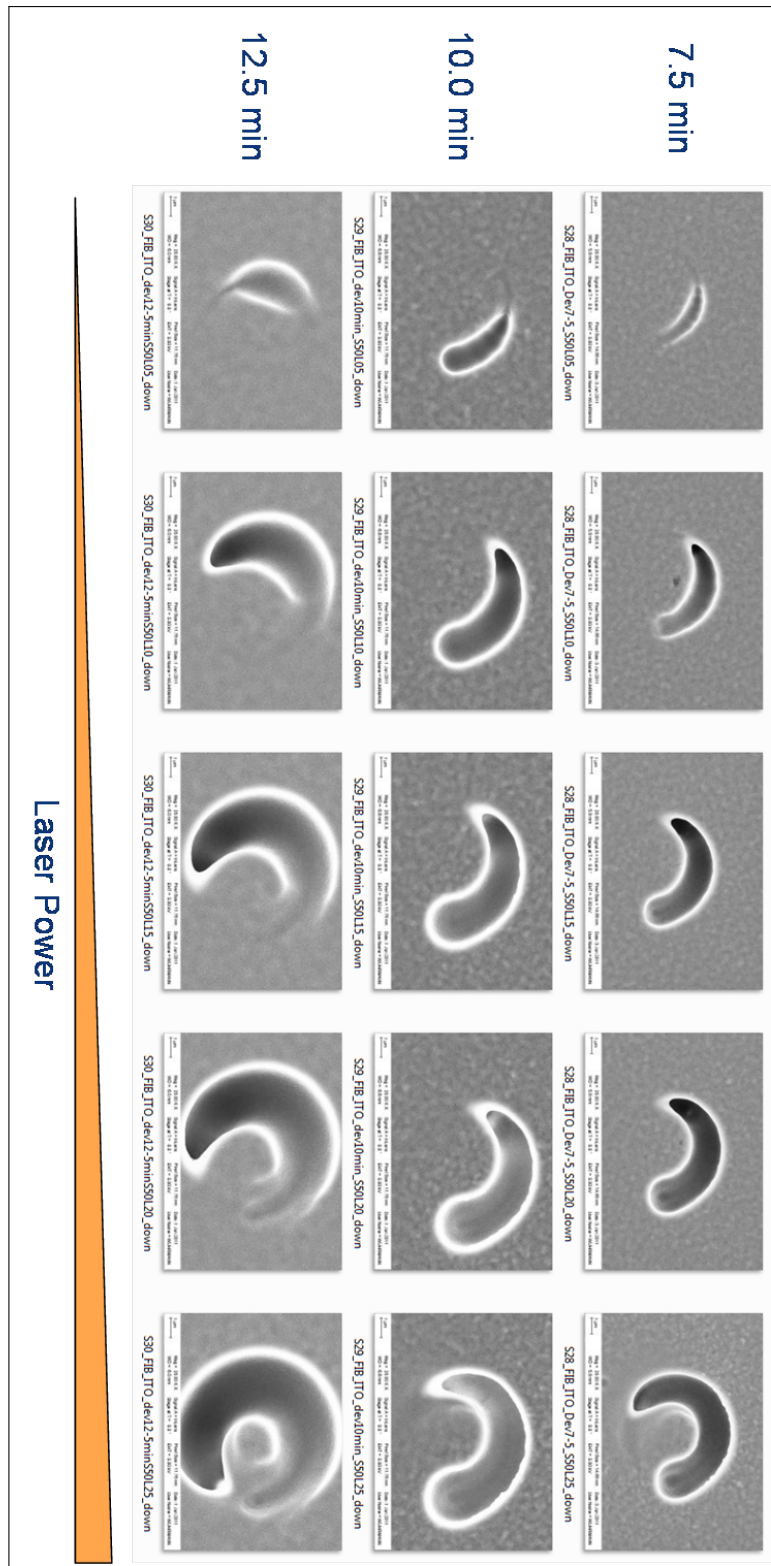
Figure 19:   *SEM top view images of helices written in downwards direction, developed in AZ826MIF for* 7.5 min, 10 min *and* 12.5 min.

(a) 7.5 min, L20   (b) 12.5 min, L25
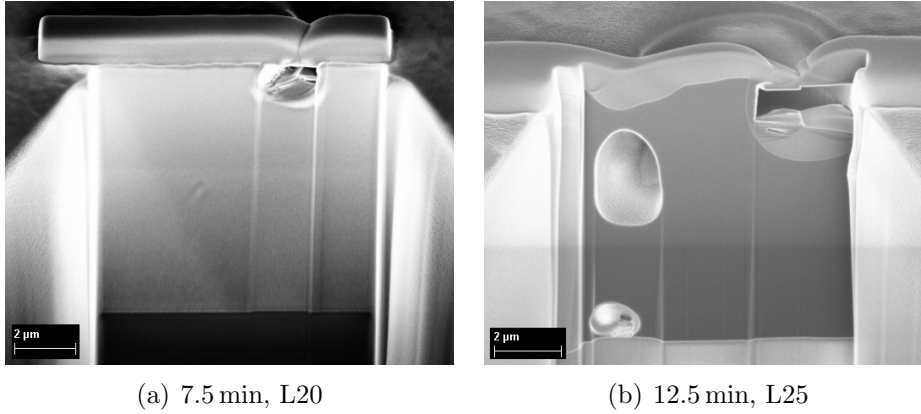
Figure 20: *FIB cuts of of helices written in downwards direction, developed in AZ926MIF for* 7.5 min *(a) and* 12.5 min *(b).*

The test runs described above have been conducted on samples with a photoresist layer of ten micrometers. An adaptation of the developing time is obviously needed when changes in the resist thickness are desired. As a rule of thump, one minute of development per micrometer resist thickness plus 2.5 min additional development (to be on the safe side) was used. This rule was tested up to resist layer thickness of 19 µm.

4.3   Determination of Electroplating Conditions

To find the best conditions for the deposition of a certain metal, structures of increasing complexity have been prepared for test runs: ETH logos with a well known area of $1000\,\mu m^2$, arrays of columns and finally the helices with a total area of approximately $1000\,\mu m^2$ again. As the charges (Q) per area (A) combined with the deposition time define the volume of deposited material the deposition time was adjusted whenever the current density (j), and therefore the applied current (J), has been changed. To compare the effects of different applied current densities (j) the charge density (q) was kept constant:

$$q = \frac{Q}{A} = \frac{j}{t} = \frac{\frac{J}{A}}{t} \tag{4.1}$$

The current densities have been increased up to the state when deposition occurs uniformly over the sample. Once the best conditions in terms of coverage have been found, the deposition time was adjusted in order to avoid overgrowth or to

achieve controlled filling of the hollow structures.

4.4   Conclusions

The parameters which have been finally chosen for the fabrication (listed in Chapter 5 were set to assure the achievement of prototypes. The influences of structure writing in up- or downwards direction or the use of other writing modes (like pulsed mode writing instead of continuous mode) were not investigated further more. Even with the writing modes chosen for the prototype writing, there is room for improvements in the detection of the lower exposure limit needed for polymerization. The laser power can be further reduced and the writing speed could be increased by a compensating the shrinkage of the helix diamterers in higher scan speeds with an increased diameter in the design. A lower laser power would result in structure filaments and the use of higher scan speeds could enable processing times needed for batch fabrication.

5   Results and Discussion

The sample preparation for the final samples as they have been used for electro-plating is described in Chapter 3. The writing parameters are listed in Table 5 for the ETH logos and Table 6 for single line structures (as helices). The parameters found for labelling have been kept for solid structure writing (and have not been optimized) while slicing distances equal or below one micrometer have been used to achieve fully developed structures. The parameters for single structure writing have been set according to the findings documented in Section 4.1. It needs to be mentioned here that the applied laser power (10%) could be reduced further more to achieve thinner filaments. It was kept below 15% to avoid interconnection of helix filaments but not reduced further more to avoid development errors due to a lack of intensity.

Table 5: Nanoscribe parameters for solid structure writing

Command	Value	Description / Remarks
PerfectShape	0	off (or on, if contours are required)
ConnectPoints	1	on
Pointdistance	50	[μm]
ScanSpeed	200	[μm/s]
Laserpower	20	[%] (with PowerScaling 1.0)

Table 6: Nanoscribe parameters for single line structure writing

Command	Value	Description / Remarks
PerfectShape	0	off
ConnectPoints	1	on
Pointdistance	50	[μm]
ScanSpeed	50	[μm/s]
Laserpower	10	[%] (with PowerScaling 1.0)

5.1   Cobalt-Nickel Helices

5.1.1   Morphology

The first helices which have been achieved were made out of cobalt-nickel. Figure 21 shows different filling grades of structures plated in only one sample. This non-uniform deposition can be explained by the fact that the sample was partly uncovered with electrolyte solution for a certain time. For the next series of

(a)   (b)
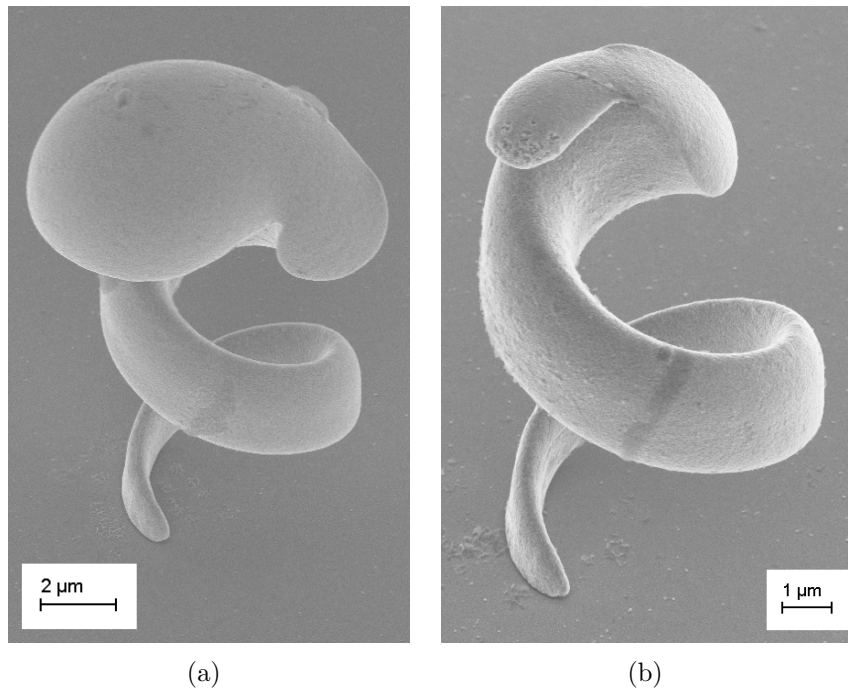
Figure 21: *SEM image of overgrown (a) and 'filled up to the top' helices (b) made out of Cobalt-Nickel (j=-22 mA/cm^2, q=300 C/cm^2)*

helices the charge density has been reduced to avoid overfilling. Due to long processing times while using -22 mA/cm^2, the current density has been increased to j=-50 mA/cm^2. This allows shorter plating times while keeping the charge density constant (see Equation 4.1 for further details). An array of the resulting structures is shown in Figure 22. All helices in this array show good reproducibility. Due to the surface tension forces which occurred during the rinsing and especially the drying procedure some of the structures are not standing in an upright position any more.
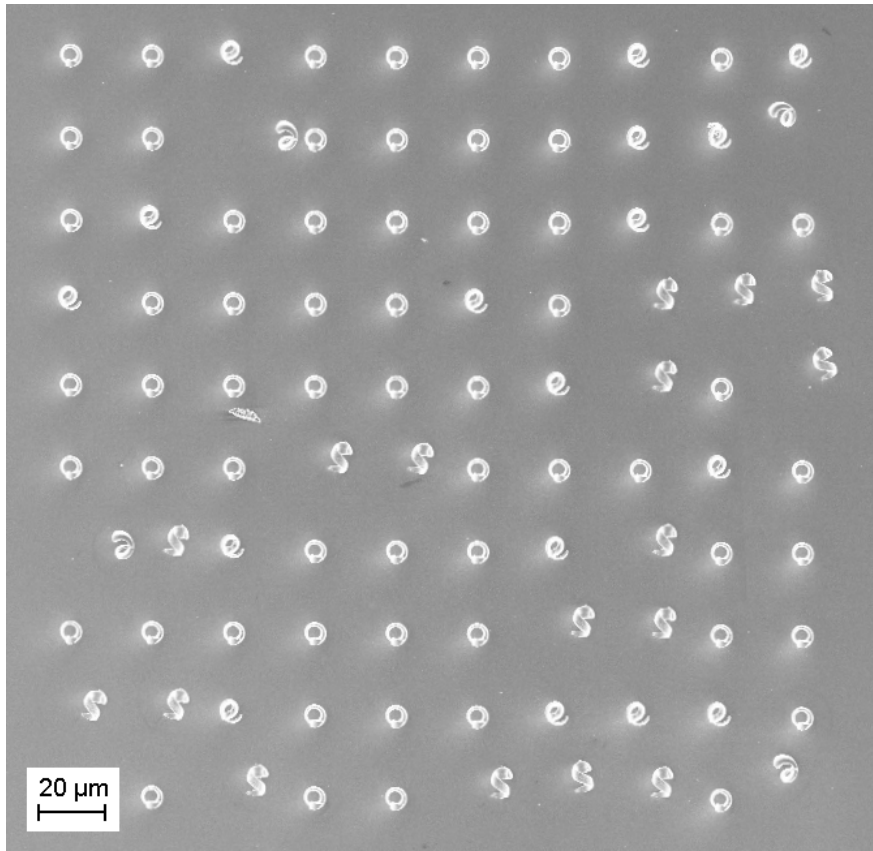
Figure 22: *10x10 array of Cobalt-Nickel helices partly laying on the substrate (j=−50 mA/cm², q=250 C/cm²)*

5.1.2   Material Composition Analysis

In Figure 23 a focused ion beam (FIB) cut of a sample of the same series as described above (j=−50 mA/cm², q=250 C/cm²) is shown. The filling of the structures is of uniform appearance. An EDX analysis of those structures showed a material composition of 49% cobalt and 51% nickel (Figure 24). (The small peak at 8.2 keV next to the strong peak of Ni, both with green markers, belongs to nickel as well.)

Magnetic films which have been plated with the identical electrolyte bath were analysed and documented in [3]. A vibrating sample magnetometer (VSM) measurement (Figure 25) was conducted. The deposits of 6 μm thickness, plated with a current density of −20 mA/cm², showed a saturation magnetization of 0.85 T (680 kA/m) and a coercivity of 1.6 kA/m (20 Oe).
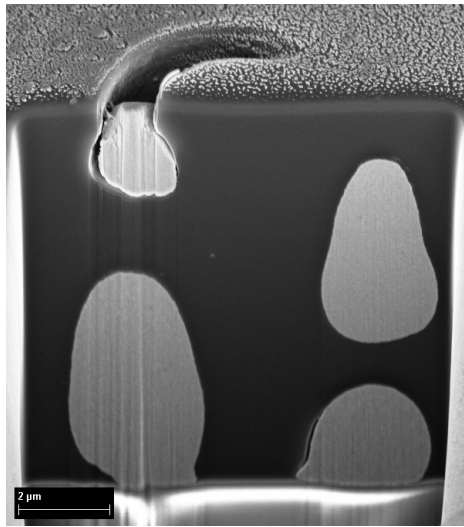
Figure 23: *Focused ion beam cut of a cobalt nickel plated helix ($j=-50\,\mathrm{mA/cm^2}$, $q=250\,\mathrm{C/cm^2}$)*

Element	Wt %	Mol %	K-Ratio	Z	A	F
CoO	48.97	48.89	0.3625	0.9398	1.0017	1.0000
NiO	51.03	51.11	0.3920	0.9747	1.0028	1.0000
Total	100.00	100.00				

EDAX ZAF Quantification (Standardless)
Oxides
SEC Table : Default
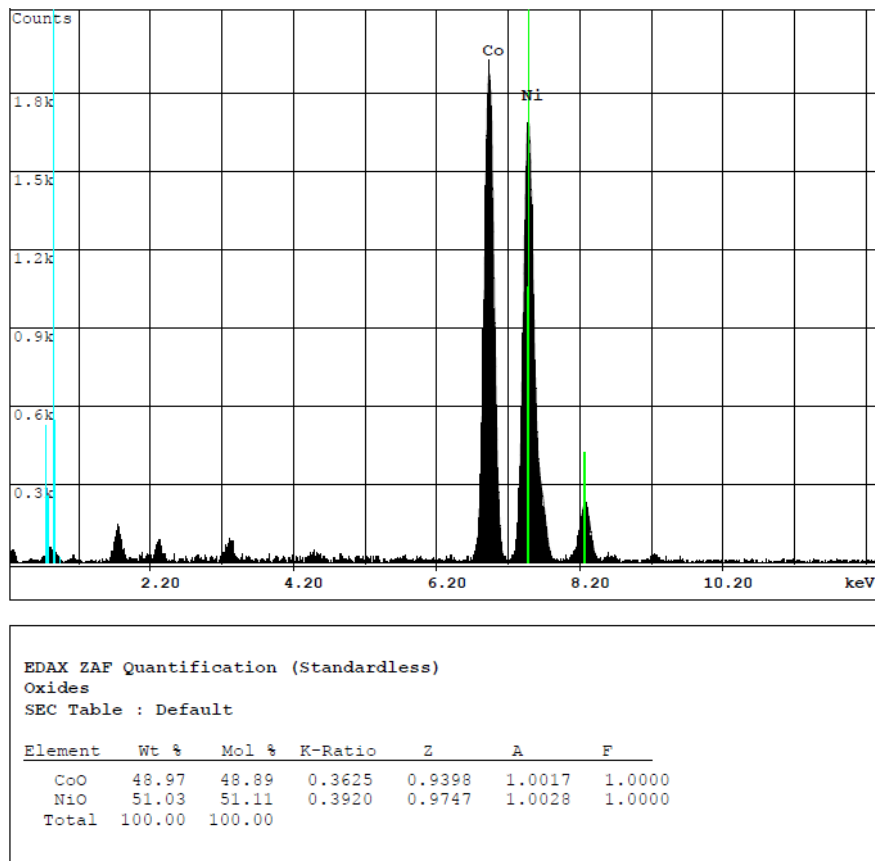
Figure 24: *EDX Analysis of the Cobalt-Nickel plated Helices ($j=-50\,\mathrm{mA/cm^2}$, $q=250\,\mathrm{C/cm^2}$)*
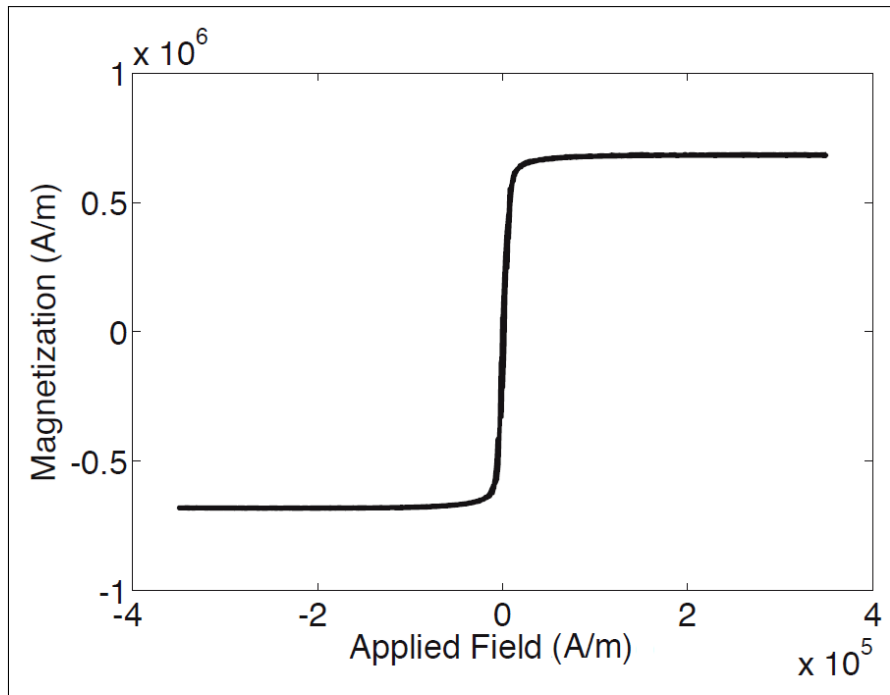
Figure 25: *VSM measurement of a* 6 μm *cobalt-nickel film electroplated with a current density of* −20 mA/cm² *([3])*

5.1.3   Magnetic Actuation

Swimming tests have been performed using the three Helmholtz coil setup described in Section 2.3. The swimming of the ABFs shown in Figure 21 (1.66 turns and overgrown) was determined to be a mixture of wobbling and corkscrew motion. The wobbling is expected to be caused by the slight overgrowth, which brings a certain lack of balance into the swimming behaviour. The best swimming results have been achieved with the 1.25-turn swimmers shown in Figure 22. The swimming was mainly corkscrew motion. In Figure 26(a)-(d) a frame sequence of an ABF in DI-water is shown to illustrate the orientation with respect to the magnetic field. Figure 26(e) shows the resulting forward motion (from top to down) of the ABF. The swimming was always accompanied by drifting (from left to right), caused by the interaction with the substrate. It has to be mentioned that the CCD camera did not provide high speed imaging and therefore one had to deal with several visual artefacts especially when using high frequencies. Therefore the corkscrew motion was possibly accompanied by a slight wobbling.

(a) 0.00 s   (b) 0.05 s   (c) 0.10 s   (d) 0.15 s

(e) time step 2.5 s   (f) CoNi ABF
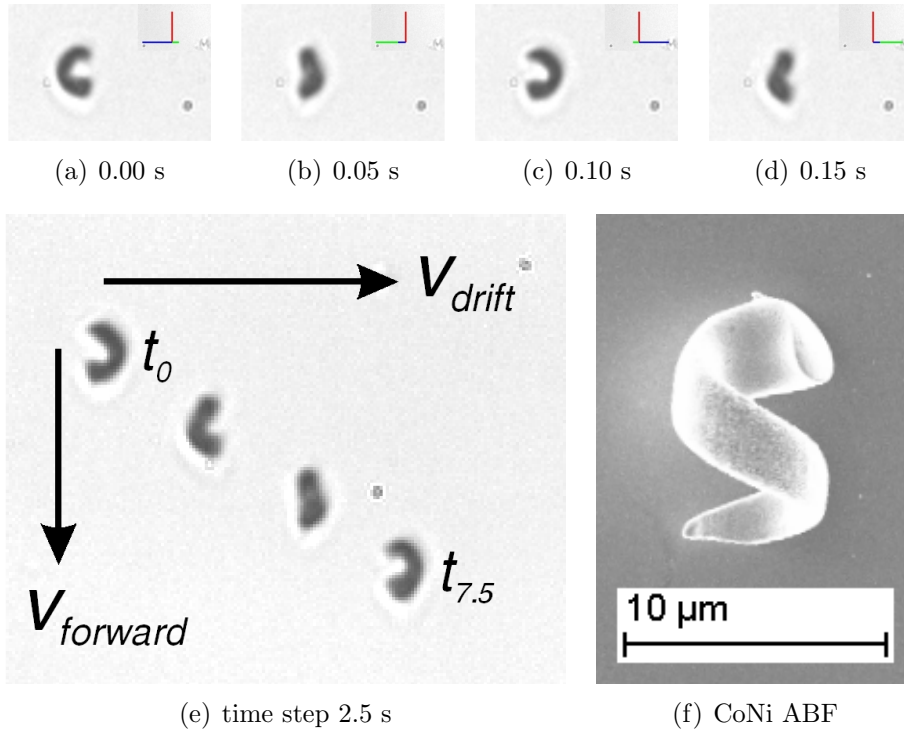
Figure 26: *(a)-(d) Frame sequence of a cobalt-nickel 1.25-turn ABF (f) swimming in DI-Water. The field is rotating along the longitudinal helix axis (green and blue vectors rotating around the red vector. (e) Overlaid images: The forward motion (from top to down) is accompanied by drifting (from left to right). (yaw=90°, pitch=0°, f=5 Hz, B=0.5 T)*

Figure 27 shows some summarized results achieved from swimming tests with these ABFs. The diagram shows the forward velocity dependence on the frequency of the rotating magnetic field. According to preliminary results with other helical microswimmers a linear dependency is recognizable. There is also a certain dependency on the swimming direction (perpendicular to the yaw) visible in the figure. It was estimated to be an artefact coming from certain offset errors in the low field strength regime. Also tilt errors within the manipulation setup might caused a certain drift due to gravity. Doubling the applied field strength lead also to an increase of velocity, approximately by a factor of 1.25.
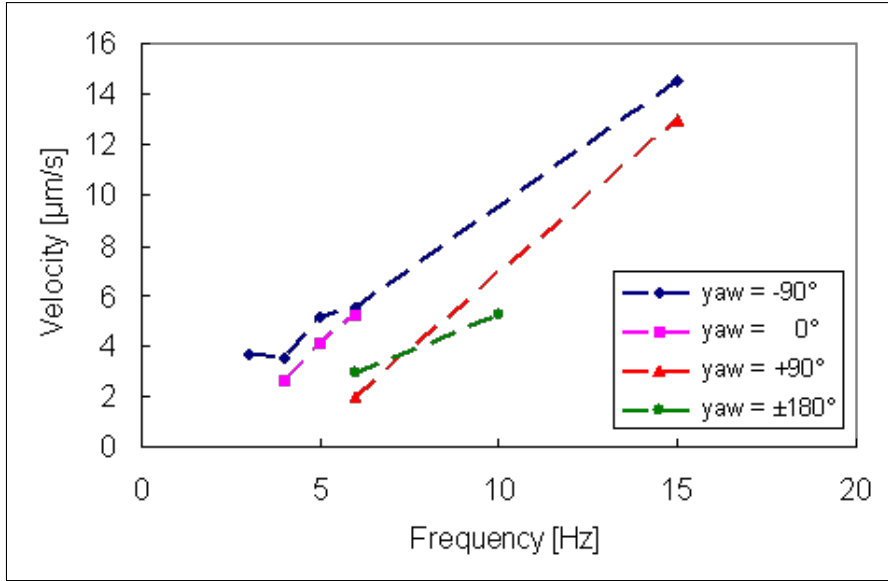
Figure 27: *Swimming results ($v_{forward}$) from a 1.25-turn cobalt-nickel ABF. (B=0.5 mT, pitch=0°)*

5.2   Iron Helices

5.2.1   Morphology

Iron was deposited in similar samples as already used for cobalt-nickel. First results were achieved by using the same plating conditions as used to plate the CoNi helices[13] (j=−50 mA/cm^2 and q=250 C/cm^2), but the plating results showed bad coverage. Usually higher current densities are used to achieve good coverage with the electrolyte bath described in Table 2 (please refer to [16] for more information). Increasing the current stepwise up to j=−150 mA/cm^2 while keeping the same charge density lead to fully covered results. Structures of such samples are shown in Figure 28. In the top region of the helices a dendritic overgrowth can be seen. This phenomenon is expected to be the result of the comparably high current densities, while in cobalt-nickel helices a mushroom like overgrowth was investigated (compare with Figure 21). It is therefore recommended to use lower charge densities to prevent the helices from overgrowing by stopping the electrodeposition before the metal filling reaches the top region. In later series of iron helices the charge density was reduced by 25 C/cm^2, or in other words the

---

[13]The decision to start with these parammeters has been taken in respect to the similar ion charging(+2) of Iron, Cobalt and Nickel.
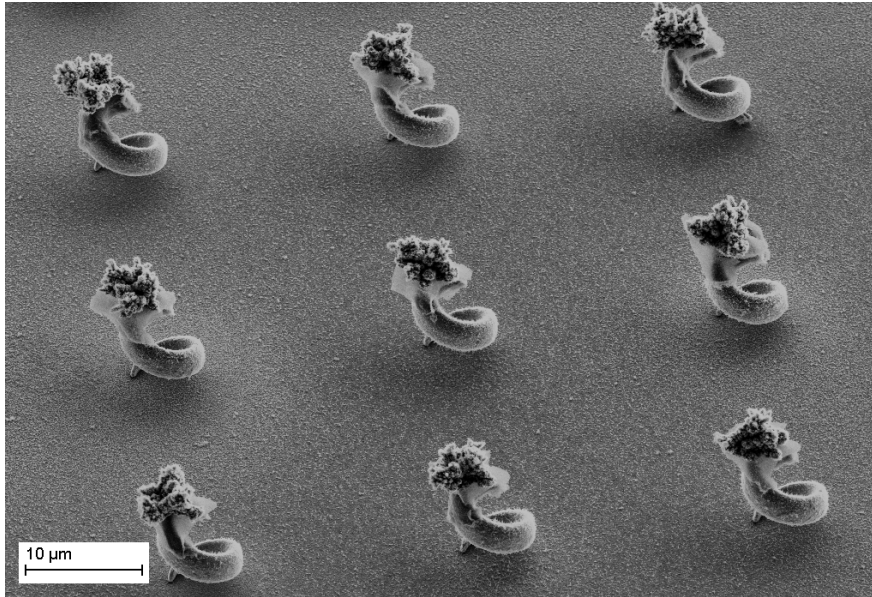
Figure 28: *SEM image of helices made out of iron (j=−150 mA/cm², q=250 C/cm²) with dendritic overgrowth in the top region of the helical structure*

plating time has been reduced.

5.2.2   Material Composition Analysis

In collaboration with the Autonomous University of Barcelona samples with iron ABFs were characterized for their material composition and magnetic properties. The deposition of iron has been proved by EDX. In some measurements there was a strong peak of oxygen indicated, which was either an oxidized structure surface or a signal remaining from the indium tin oxide coating underneath. On a sample with 5000 helical structures (approximately $2.5\,\mu$ magnetic material) a VSM measurement has been conducted in perpendicular-to-plane conditions. The resulting hysteresis loop is shown in Figure 29. The iron deposits plated with a current density of $-150\,\mathrm{mA/cm^2}$, showed a coercivity of $11.1\,\mathrm{kA/m}$ (140 Oe). By estimating the volume[14] of one helical structure to be around $200\,\mathrm{\mu m^3}$ and concerning full coverage (5000 structures) and uniform plating results a saturation magnetization of around ($1700\,\mathrm{emu/cm^3}$) was calculated which corresponds to the tabulated value for iron. The amount of iron on the sample was not measured

---

[14]Volume calculation of a one turn helix CAD model (idealized round filament, diameter $2.5\,\mathrm{\mu m}$) and a cone representing the overgrowth
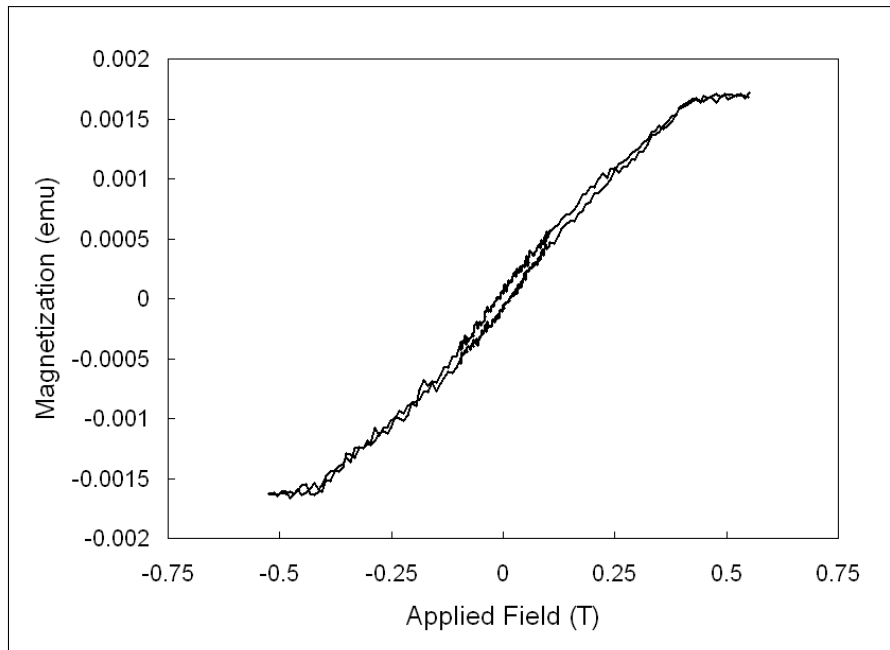
Figure 29: *Hysteresis loop from a VSM measurement on a sample with 5000 iron helices measured perpendicular to the substrate*

concerning the low amount of deposit on the sample (approximately 5 m) and possible losses during the removal of the photoresist.

5.2.3 Magnetic Actuation

The Iron helices described above have shown comparable swimming behaviour as observed for CoNi helices of the first series. Figure 30(a)-(d) shows the frame sequence of an iron ABF with dendritic overgrowth swimming in deionized water. The orientation of the ABF with respect to the magnetic field is illustrated: Possibly caused by the overgrowth, the corkscrew swimming motion was superimposed by wobbling.

5.3 Structural Designs for Biochemical Functionalization

In order to improve the applicability for biochemical applications two different concepts have been followed. The first one is based on the ABFs made from cobalt-nickel as described in Section 5.1. By adding a gold head on the top of the helices a hybrid metal structure which is capable for magnetic driven propulsion

(a) 0.00 s   (b) 0.05 s   (c) 0.10 s   (d) 0.15 s
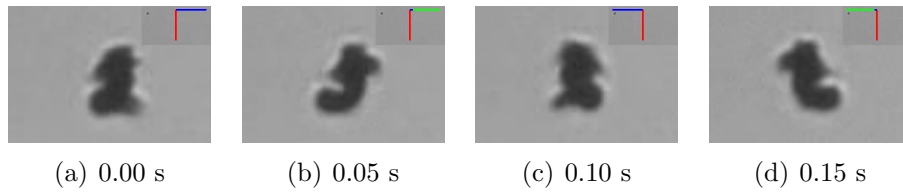
Figure 30: *(a)-(d) Frame sequence of a iron 1.25-turn ABF (f) with dendritic overgrowth, swimming in DI-Water. The field is rotating along the longitudinal helix axis (green and blue vectors rotating around the red vector. (yaw=−90°, pitch=0°, f=5 Hz, B=0.5 T)*

(CoNi) as well as biofunctionalization (Au) is generated.[15] The second concept is based on iron helices (Section 5.2) for the propulsion. Coating the structures with layers of carbon enables them for biochemical functionalization[16].

5.3.1 Bacteria-like Hybrid Metal Structures

In the top region of the helices a section with reduced pitch of one micrometer has been added. The goal of this change in shape was a controlled overgrowth, centred over the helix axis. Some preliminary results are shown in Figure 31. The defined head has been written in the region right before the mushroom-like overgrowth occurred. As the written head takes about one to two micrometers of possible writing height (limited by the photoresist thickness), the maximum length of the helices is reduced by that as well. A reduced radius of two micrometers and a pitch of four micrometers have been used to achieve more turns in that part of the structure where the helix is written. In this case the helix filaments are no longer separated from each other. Possible methods to achieve structures without interconnections are discussed in Section 5.4.

The second series of bacteria-like structures have then been fabricated by starting with one full turn of a cobalt-nickel helix (j=−50 mA/cm^2, q=225 C/cm^2) and a subsequent electrodeposition of gold (j=−10 mA/cm^2, q=5 C/cm^2). For the electroplating of gold the increased plating area in the top region of the structures, namely the area of the written head, needs to be counted in. In Figure 32 the identical structure is inspected using two different SEM detectors: Figure 32(a) was imaged using the inlens detector, mainly focussing on structural

---

[15]An example for biofunctionalization of gold can be found in [11]

[16]An example for biofunctionalization of carbon can be found in [12]
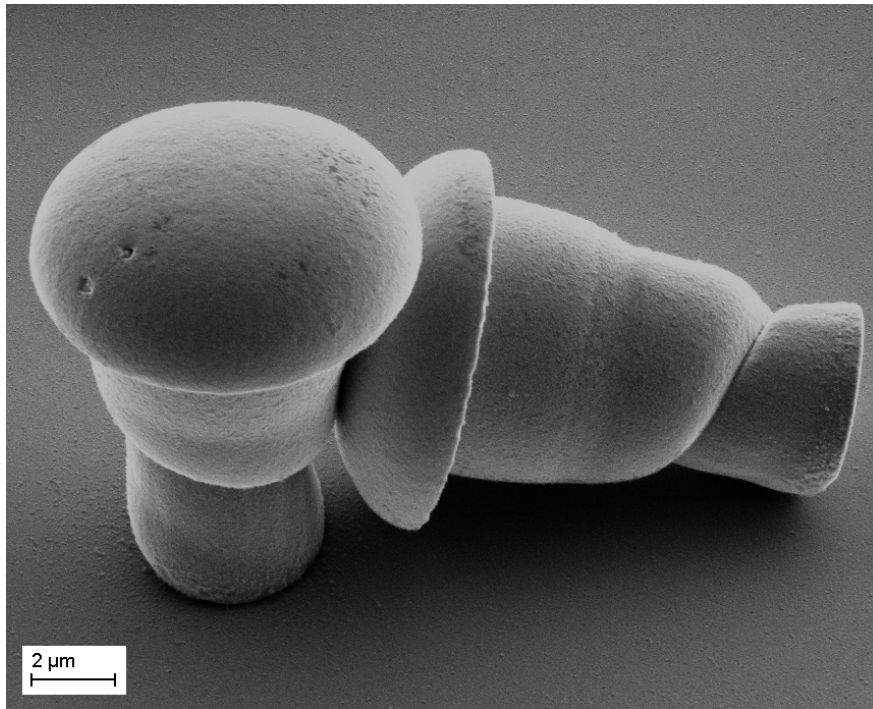
Figure 31: *SEM image of bacteria-like structures made from Cobalt-Nickel helices with controlled overgrowth (j=$-50\,\mathrm{mA/cm^2}$, q=$250\,\mathrm{C/cm^2}$)*

features while in Figure 32(b) the material contrast is highlighted by the use of the ESB detector. The deposition of different materials (bright gold head, dark cobalt-nickel tail) had additionally been proved by EDX analysis.

5.3.2   Outlook: Carbon Coated Iron Helices

In ongoing research on metal nanowire encapsulation with carbon[17], iron acts as catalyst in a chemical vapor deposition (CVD) process for carbon deposition. This would allow the selective coating of the iron helices with carbon layers. First trials for the temperature resistance of the substrates showed problems with the glass substrates. For the deposition of carbon, temperatures of around $750\,°\mathrm{C}$ are required. This was already close the temperature where softening of the glass occurred. Furthermore temperature gradients arising from different materials (the wafers have been put on silicon wafers) caused cracks and finally broken samples. Writing the helical structures on quartz wafers would be one option to achieve temperature stable samples without changing to much parameters in the

---

[17]Conducted by Muhammad Arif Zeeshan IRIS, Swiss Federal Institut of Technology

(a) SEM: Inlens   (b) SEM: ESB
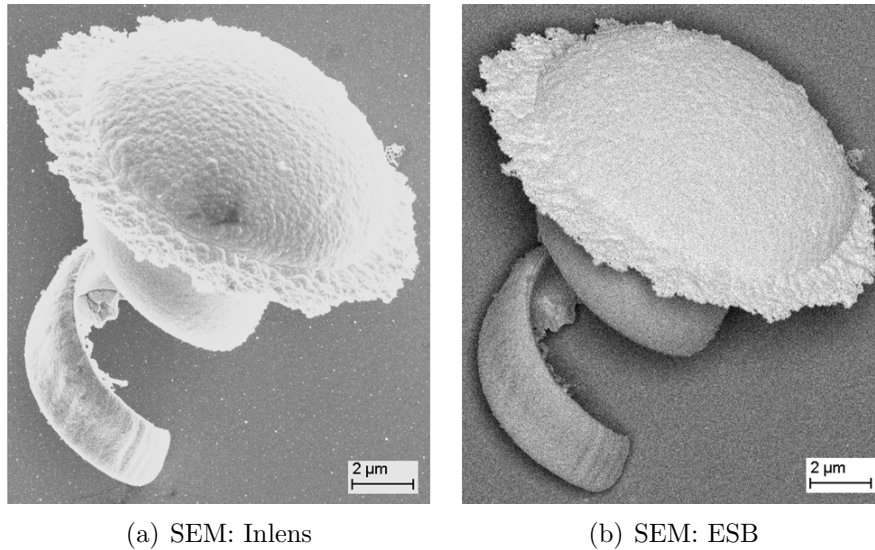
Figure 32: *SEM images of hybrid structures composited by cobalt-nickel helices (j=50 mA/cm^2, q=225 C/cm^2) and additional deposition of gold (j=$-$10 mA/cm^2, q=5 C/cm^2) on the top. Structural information is achieved by the use of an inlens detector (a) and material contrast by an ESB detector (b).*

fabrication process.

5.4 Design Modifications

As already mentioned in Section 5.3 for future work on those designs there will be a strong need to achieve structures with longer helical tails respectively tails with more helical turns. While keeping the same pitch/radius ratio constant there are two possible ways to follow: (I) Increasing the photoresist thickness or (II) downscaling of the designs. This section is discussing the limits of those approaches.

5.4.1 Increasing the Photoresist Thickness

The thickness of the photoresist layer has been increased up to a thickness of 19 μm. For these target thicknesses double layer spincoating was conducted according to the recipe in Appendix A. Figure 33 shows cobalt-nickel structures plated in 19 μm templates. It can be seen that a non-uniform deposition occurred. This was expected to be caused by increased hydrogen evolution during electroplating. Increasing the nitrogen bubbling showed immediate reaction in
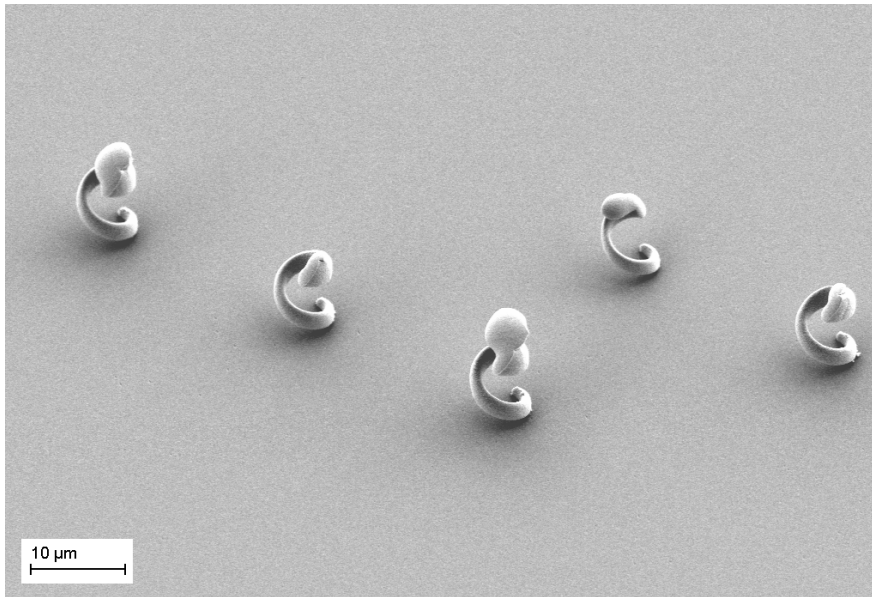
Figure 33: *SEM image of ABFs deposited in* $19\,\mu m$ *templates.* $(j{=}{-}50\,mA/cm^2,$ $q{=}350\,C/cm^2)$

terms of stabilized voltage response. By increasing the applied current one could achieve a faster seed layer growth for better uniformity, but this would force the formation of hydrogen bubbles one more time. Another approach to overcome this problem could be the use of pulsed electroplating, where a rest phase in between the current pulses is added.[18]

In Figure 33 it is furthermore visible that the filament diameter of the helical structures keeps constant over the whole ABF body. For the used template bacteria shaped pores have been written to achieve more uniform developing results. The used developer AZ826MIF shows strong grey erosion due to the additives for scum free developing and therefore widening of the upper parts of the helix will occur. For the same reason the resulting template thickness will be less than the spincoated thickness. In the previously presented ABFs as shown in Figure 21 and 22 this effect was clearly visible as the used templates $(10\,\mu m)$ have been filled up to the top. Profilometry measurements showed that after 20 minutes of developing with AZ826MIF already one micrometer of unexposed resist had been removed. After 30 minutes developing, the surface became rough and an erosion of around 3.5 micrometers was measured.

---

[18]An example of pulsed electroplating and a discussion of the effects can be found in [16].

Magnetic actuation tests on the structures visible in Figure 33 showed mainly tumbling motion. Referring to [13] a possible explanation could be found in the higher volume of magnetizable material, leading to a tendency to tumbling motions already within low field strengths. Remembering the mentioned errors on lower field strengths, decreasing the power hence lead to non-defined swimming motions. Also due to the increased amount of magnetic material a kind of corkscrew motion could only be observed using high frequent rotations (more than 30 Hz). Once more this statement need to be taken with care, as there was no high speed camera installed to observe such fast motions.

5.4.2   Downscaling

The more interesting way to achieve more helical turns would be downscaling of the structures. By downscaling more structures could be written next to each other and the writing duration could be reduced due to the shorter paths. As already described in Section 2.1 this approach is mainly limited by the optical resolution but also dependent of the material selection. Figure 34 and also Figure 31 show the results of downscaled structures with a radius of two micrometers and a pitch of four micrometers. The filaments seem to be separated from each other only in the bottom part of the structure. Due to the increased thickness of the filaments in the top part of the templates (due to increased dark erosion) interconnections are forced to occur in these regions.

There are two ways to improve the downscaling: (I) The laser power could be decreased further more and (II) one could use a different developer. According to [1] AZ726MIF works with similar composition as AZ826MIF except that no additives for scum free development are added. By using the AZ726MIF developer, results with less dark erosion occurring could be expected.[19]

---

[19]A few tests with another basically compatible developer ([1]), the AZ400K (diluted 1:4 for fast development), have been conducted. The results showed strong tendency to crack formation and underetching of the structures.
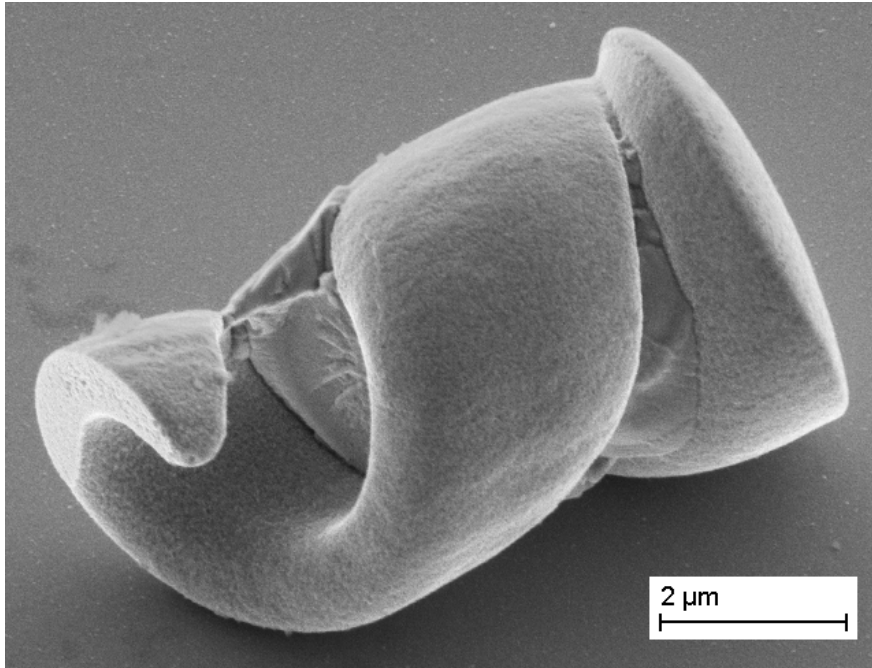
Figure 34: *SEM image an ABF with a radius of two micrometers and a pitch of four micrometers. ($j=-50\,\mathrm{mA/cm^2}$, $q=250\,\mathrm{C/cm^2}$)*

5.5 Conclusions

Cobalt-nickel helices The best swimming behaviour, namely pure corkscrew motion, was achieved with ABFs of the second series. These structures had a non-symmetric mass distribution, starting with filament diameters of around 1.5 micrometer in the bottom part and ending in filaments with more than 2.5 micrometer thickness. Comparing the wobbling and corkscrew motion swimming results of the first cobalt-nickel swimmers (1.66-turn swimmers with overgrowth and non-symmetric mass distribution) with the observed tumbling motion described for the helices of the third series (1.66-turn swimmers with symmetric mass distribution) lead to additional conclusions. The non-symmetric shape might enforce wobbling motions but also seems to help the change into corkscrew motion respectively avoiding tumbling. These effects have been observed in plane swimming on the substrate. Therefore ground effects can be expected which could lead to different swimming behaviour than for free 3-D swimming.

Iron helices Helical structures made from iron have been fabricated as a basis for carbon coated ABFs regarding future biochemical functionalization. The iron ABFs have not been optimized for good swimming results due to the fact that a further reduction of the deposition time would have resulted in helices with less than one turn. Design modification like downscaling would provide templates with longer pores compared to the desired amount of deposit and could prevent the structures from the overplating. The (dendritic) overgrowth occurred earlier than within cobalt-nickel deposition while keeping the same amount of charge densities. This phenomenon is mainly expected to be caused by the three times higher applied current density which enforces to build dendritic structures into the electrolyte bath.

Structural designs for biochemical functionalization The introduced structural designs are meant to inspire future projects on ABFs as well as other projects with similar set objectives. To achieve these designs, templates with already achieved fabrication parameters have been used as they were identified for cobalt-nickel or iron helices. To meet the requirements for special applications as well as for optimization of the swimming behaviour changes in the designs will be needed.

Design modifications For future work, modifications like increasing the photoresist thickness, decreasing the laser power or using another developer should only be taken into account if there are special requirements for new designs. Every change in these parameters will effect the subsequent electrodeposition in several parameters. Especially the current and the charge density would be needed to modify whenever different diameters of the helices are provided with freshly designed templates. Every new design should therefore be carefully designed before the fabrication of new templates starts. Changes during the experimental parameter identification as described in Chapter 4 would disturb the systematics and might necessitate a complete repetition of certain steps. It needs to be pointed out that this is not only valid for design modifications but also for every change in preliminary fabrication steps (choice of substrate, conductive layer thickness, etc.).

6   Summary and Contributions

Artificial bacterial flagellum (ABF), a helical microrobot, has potential to act as a biomedical robot for *in vivo* and *in vitro* applications such as targeted drug delivery, microsurgery, cell manipulation and single-cell analysis. In this work the design, fabrication and characterization of metallic ABFs was reported. Ferromagnetic structures, including CoNi, Fe and hybrid structures were obtained using 3-D laser lithography and electrochemical deposition. Ferromagnetic helical devices are promising for applications in highly viscous fluid environments, such as bio-fluids. Once functionalized, they have the potential to perform targeted delivery of energy (e.g., inductive heating) as well as chemical and biological substances.

The fabrication processes of ferromagnetic ABFs can be summarized by the following steps. First, a bare glass substrate is coated with an indium tin oxide (ITO) layer by e-beam evaporation. Then a positive tone photoresist (AZ9260) is spin-coated on the thermally treated ITO samples. Based on two-photon polymerization technique, 3-D lithographic patterning of hollow helical-shaped structures are performed using a direct laser writing tool (provided by Nanoscribe GmbH). These substrates with vertical arrays of helical pores are then filled by electrochemical deposition with a CoNi alloy, Fe or multiple segments of different metals. Finally the freestanding ferromagnetic helical structures are obtained by removing the photoresist template.

The morphology and material properties of the metallic ABFs were investigated by SEM, EDX and FIB. Magnetic measurements have been performed using VSM (for CoNi) and MOKE (for Fe).

Magnetic actuation tests were conducted in deionized water using a uniform rotating magnetic field. The results show that the metallic ABFs are capable of performing corkscrew motion and navigation in fluid. The best swimming results have been achieved with 1.25-turn CoNi swimmers. The velocities reached showed linear response to the applied frequency of the rotating field. The maximum velocity before the step out frequency would be reached is expected to be more than $30\,\frac{\mu m}{s}$. At such high frequencies no more clear observation and measurements could be performed using the CCD Camera which was attached to the microscope. Compared to previously reported ABFs consisting of soft-magnetic heads and helical ribbon tails ([19]) and magnetic polymer based ABFs ([13]),

larger magnetic torques can be generated for magnetic actuation due to a much larger volume of the magnetic material. The field strength to actuate the structures was kept at 0.5 mT. This field strength turned out to be the lower limit of the acutation setup before the applied fields became non-uniform.

Two approaches of structural designs for bio-/chemical functionalization of the ferromagnetic ABFs have been described. (I) helical structures consisting of two or multiple segments of metals, such as Au and CoNi alloy; (II) encapsulation of ferromagnetic ABFs with carbon layers by a CVD process. The ferromagnetic multi-segment ABFs have been obtained by successive electroplating. They were bacteria-like shaped with a magnetic (CoNi) helical tail and a functionalizable (Au) head. The carbon coated ferromagnetic ABFs were based on iron helical cores which would act catalytic during the carbon coating process. Both concepts have been introduced as a basis for future projects.

Another major goal, the combination of ongoing research fields (ABFs and ferromagnetic nanowires), was achieved successfully. The initialization of the production of complex 3-D shaped structures using the presented fabrication process techniques, opened a wide range of possibilities to the Institute of Robotics and Intelligent Systems. This project opened up minds for multiple new ideas which could not be realized with conventional microfabrication methods.

6.1 Future Work

For certain applications a better conductivity and transparency of the ITO layer might be needed. Changes in the deposition technique like evaporation in oxygen rich environments and resistivity, respectively transparency tests up to 500 (or higher temperatures) should be performed for the improvement of the material properties.

Special holders for proper cover glass handling are just provided for rinsing and developing. For the evaporation of ITO improvements on the sample attachment (like the use of masks) would help to avoid cracks in the substrates. Therefore the yield of intact samples for the further fabrication could be improved. Furthermore the use of the lift-off tape could be replaced by partial exposure (e.g. on a mask aligner) for a photolithographic removal.

Another option is the complete replacement of the glass wafers with other substrates. The use of quartz wafers (which generally have less defects as the

used glass coverslips) might lead to a better sample yield and would additionally provide better thermal stability (such as a higher softening and melting point which is feasible for the CVD processing). Quartz wafers are not expected to cause significant changes in the writing parameters. The use of mechanically more stable (but usually non-transparent) substrates would require several adjustments in the direct laser writing step.

The influences of structure writing in up- or downwards direction and the use of other writing modes (like pulsed mode writing) should be investigated further more. For every mode the detection of the lower exposure limit needed for polymerization should be found for the highest resolution writing. For a batch fabrication of ABFs shorter writing durations are required. To increase the writing speed, tests for higher scan speeds with a compensation of the helix diameter shrinkage could be performed. The use of the weak interface (glass-photoresist) would furthermore allow to skip the frequently performed tilt corrections within writing. Therefore the total writing duration can be reduced significantly.

For a complete analysis of the swimming behaviour of metallic ABFs, a higher number of turns, different helicity angles and multiple shapes should be studies. Therefore it will be necessary to perform some more experimental parameter identification runs on lower laser power. In parallel the use of the developer AZ726MIF is recommended although the developing times might need to be reinvestigated. Both methods will contribute to thinner helix filaments which allows more design flexibilities.

Helices with higher aspect ratios and thinner filaments might cause problems in the electrodeposition steps. This will be especially the case if the photoresist thickness would additionally be increased parallel to downscaling of the structures. To overcome those problems either higher current densities in DC-electroplating could be used or other modes like pulsed electroplating needs to be considered. As the material properties of the resulting structures (and maybe even the magnetic properties) will be different to DC-plated structures, it would be interesting to achieve helices by pulsed plating as well.

References

[1] Microchemicals gmbh, application notes. *http://www.microchemicals.eu/ technical_information/*, 31. 03. 2011.

[2] Yces - case western reserve university. *Electrochemistry Encyclopedia / Dictionary*, http://electrochem.cwru.edu/encycl/, 02. 09. 2011.

[3] O. Ergeneman. Wireless actuation and readout of magnetic biomicrosystems. *Dissertation*, Swiss Federal Institut of Technology, 2011.

[4] J. K. Gansel, M. Thiel, M. S. Rill, M. Decker, K. Bade, V. Saile, G. von Freymann, S. Linden, and M. Wegener. Gold helix photonic metamaterial as broadband circular polarizer. *Science*, 325:1513, 2009.

[5] T. Ishida, H. Kobayashi, and Y. Nakato. Structures and properties of electron-beam-evaporated indium tin oxide films as studied by x-ray photoelectron spectroscopy and work-function measurements. *Journal of Applied Physics*, Vol. 73(9):4344–4350, 1993.

[6] H. Löbl, M. Huppertz, and D. Mergel. Ito films for antireflective and antistatic tube coatings prepared by d.c. magnetron sputtering. *Surface and Coatings Technology*, Vol. 82:90–98, 1996.

[7] D. Mergel. Dünne ito-schichten als leitfähige, transparente elektroden. *Vakuum in Forschung und Praxis*, 16(2):58–61, 2004.

[8] H. Morikawa and M. Fujita. Crystallization and electrical property change on the annealing of amorphous indium-oxide and indium-tin-oxide thin films. *Elsevier - Thin Solid Films*, Vol. 359:61–67, 2000.

[9] N. V. Parthasaradhy. Practical electroplating handbook. *Prentice-Hall, Inc.*, 1989.

[10] K. E. Peyer, L. Zhang, B. E. Kratochvil, and B. J. Nelson. Non-ideal swimming of artificial bacterial flagella near a surface. *Proc. of IEEE International Conference on Robotics and Automation (ICRA)*.

[11] D. Shenoy, W. Fu, J. Li, C. Crasto, G. Jones, C. DiMarzio, S. Sridhar, and M. Amiji. Surface functionalization of gold nanoparticles using hetero-bifunctional poly(ethylene glycol) spacer for intracellular tracking and delivery. *International Journal of Nanomedicine*, 1(1):5157, 2006.

[12] M. Shim, N. W. S. Kam, R. J. Chen, Y. Lia, and H. Dai. Functionalization of carbon nanotubes for biocompatibility and biomolecular recognition. *Nano Letters*, 2 (4):285–288, 2002.

[13] E. C. Siringil. Fabrication and characterization of magneitc polymer-based artifical bacteria flagella. *Master Thesis*, Swiss Federal Institut of Technology, 2011.

[14] F. M. Smits. Measurement of sheet resistivities with the four-point probe. *The bell system technical journal*, pages 711–718, 1957.

[15] M. Thiel. Design, fabrication, and characterization of three-dimensional chiral photonic crystals. *Dissertation*, Karlruher Institut für Technologie (KIT), 2010.

[16] T. Wuhrmann. Growth and characterization of magnetic nanowires using template based electroplating. *Semester Thesis*, Swiss Federal Institut of Technology, 2010.

[17] A. M. Zeeshan, K. Shou, S. Schuerle, E. Pellicer, S. Pan, J. Sort, K. Sivaraman, S. Fusco, S. Muntwyler, M. D. Bar, and B. J. Nelson. Ferromagnetic nanowires as potential drug-delivery wireless nanorobots. *Proc. of IEEE International Conference on Nano/Molecular Medicine and Engineering, HongKong/Macau*, 2010.

[18] L. Zhang, J. J. Abbott, L. X. Dong, B. E. Kratochvil, D. J. Bell, and B. J. Nelson. Artificial bacterial flagella: Fabrication and magnetic control. *Applied Physics Letters*, 94(6), 2009.

[19] L. Zhang, J. J. Abbott, L. X. Dong, K. E. Peyer, B. E. Kratochvil, H. X. Zhang, C. Bergeles, and B. J. Nelson. Characterizing the swimming properties of artificial bacterial flagella. *Nano Letters*, 9(10):3663–3667, 2009.

[20] L. Zhang, Y. Lu, L. X. Dong, R. Pei, J. Lou, B. E. Kratochvil, and B. J. Nelson. Noncontact manipulation of ni nanowires using a rotating magnetic field. *Proc. in the 9th IEEE Conf. on Nanotechnology (NANO2009), Genoa, Italy*, 2009.

[21] L. Zhang, K. E. Peyer, and B. J. Nelson. Artificial bacterial flagella for micromanipulation. *Lab on a Chip*, 10:2203–2215, 2010.

A   Spincoating of AZ9260

A.1   Recipe for Single Coating ($6.5 - 15\,\mu m$)

The following recipe (Table 7) desribes can be used to coat layers from 6.5 up to
$15\,\mu m$ thickness.

Table 7: Recipe for single coating of AZ9260 (for $6.5 - 15\,\mu m$)

Process step	Parameter		Remarks
Coating	Dispense:	500 µl	Target film
	Spin:	*'SPIN SPEED'* rpm , 60 sec	thickness
	Acceleration:	2000 rpm/sec	9 µm
Soft bake	Hotplate:	110 °C, 165 sec	

By adjusting the spin speed accordingly to the graph in Figure 35[20] the thick-
ness can be varied. The accuracy of this graph even for the present wafers has
been proved in testruns (the results are visible in Figure 36).
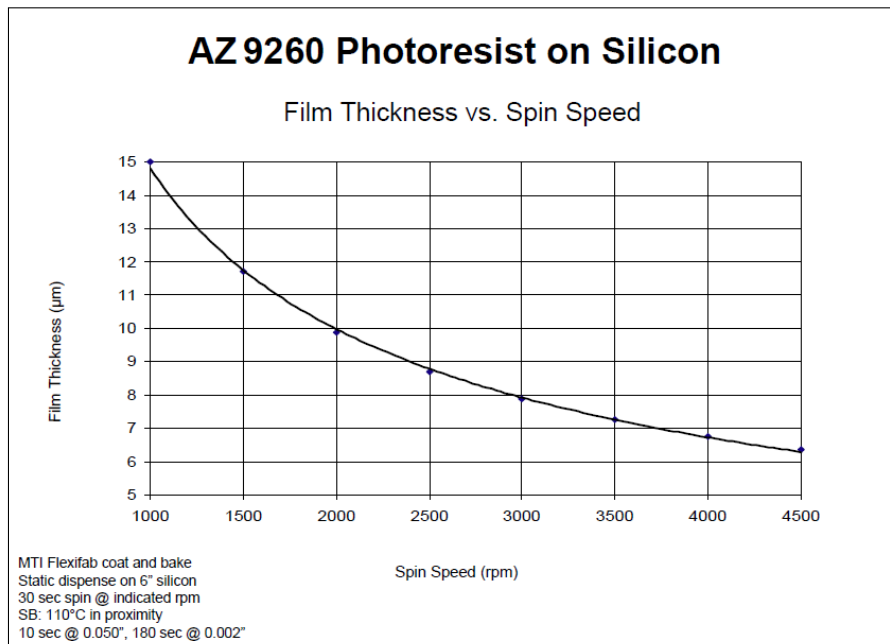
Figure 35: *Achievable thickness by single coating of AZ9260 (values for silicon
substrate) photoresist*

---

[20]`http://www.nanofab.utah.edu/svn/public/documents/Non%20SOPs/Photoresist/az_`
`9260_photoresist.pdf` 29.03.2011

A.2   Recipe for Double Coating $(20 - 33\,\mu\text{m})$

For thicknesses of more than $15\,\mu\text{m}$ several double layer coating testruns have been conducted. Table 8 contains the recipe used for layers from 20 to $33\,\mu\text{m}$.

Table 8: Recipe for double coating of AZ920 (for $20 - 33\,\mu\text{m}$)

Process step	Parameter		Remarks
1st coat	Dispense: Spin: Acceleration:	500 µl 2500 rpm , 60 sec 2000 rpm/sec	Target film thickness: 9 µm
1st soft bake	Hotplate:	110 °C, 80 sec	
2nd coat	Dispense: Spin: Acceleration:	500 µl 'SPIN SPEED' rpm , 60 sec 2000 rpm/sec	Target film thickness: 20-33 µm
2nd soft bake	Hotplate:	110 °C, 160 sec	
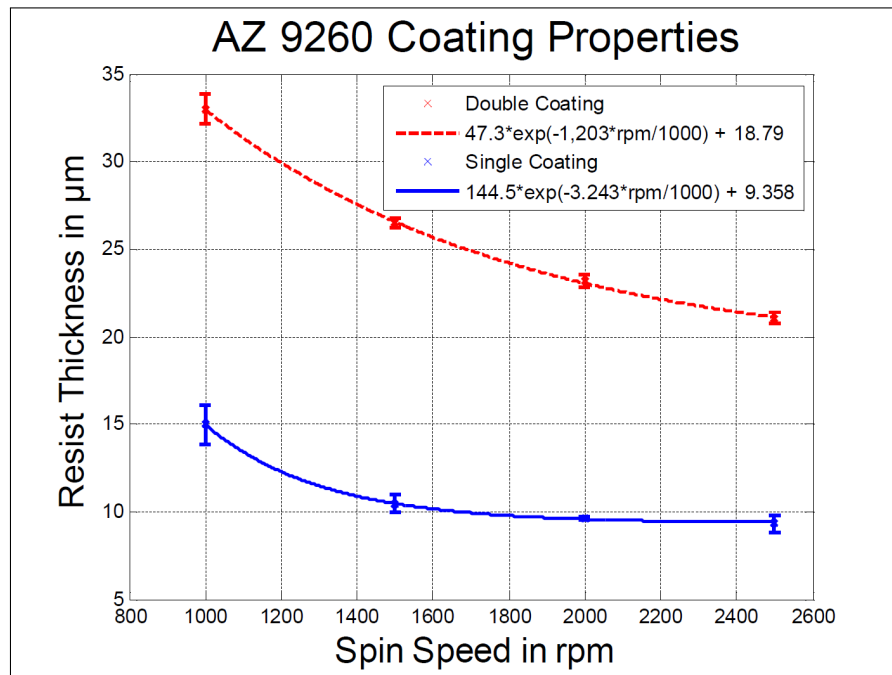
Figure 36: *Results of AZ9260 Single and Double Coating Testruns*

In Figure 36 the results of double layer coating according to the recipe above are visualized. Two more measurements have been conducted to achieve $16.8\,\mu\text{m}$ (2 x 4000 rpm) and $19.0\,\mu\text{m}$ (2 x 3000 rpm).

B   Direct Laser Writing

This chapter includes examples on the programming of helix (or bacteria) arrays (MATLAB) and how to include the predefined array files into DeScribe programs. Furthermore additional features like multiple sample writing are explained.

B.1   MATLAB Programming (m-code)

To generate the files containing predefined scanning paths of whole helix arrays, MATLAB scripts as shown in the following example has been used. The first m-code is used to assemble structures into arrays. The arrays are limited to the writing limitations of the piezo stage in x- and y-direction. The output of those MATLAB scripts is stored in the file format as used in the programming tool DeScribe (see Section B.2).

```matlab
1  %%%%%%%%%%%%%%%%%%%%%%%%%%%%%%%%%%%%%%%%%%%%%%%%%%%%%%%%%%%%%
2  %%%%%%%%%%%%          helix_assembly.m          %%%%%%%%%%%%
3  %%%%%%%%%%%%%%%%%%%%%%%%%%%%%%%%%%%%%%%%%%%%%%%%%%%%%%%%%%%%%
4
5  % 'helix_assembly' computes the coordiantes of a helix array
6  % and stores the path to be written in a gwl-file
7  % (including start/stop commands).
8
9  clear all;
10 clc
11
12 % Helix parameters
13 turns = 3;              % Number of Helix turns
14 pitch = 6;              % Helix pitch[um]
15 radius = 3;             % Helix radius [um]
16 ppt = 30;               % "points per turn" [-]
17
18 % Array parameters
19 Xoffset = 37.5;         % X axis offset from lower left array ...
       corner [um]
20 Yoffset = 37.5;         % Y axis offset from lower left array ...
       corner [um]
21 AddXoffset = 25;        % X offset in between helix ground ...
       points [um]
22 AddYoffset = 25;        % X offset in between helix ground ...
       points [um]
23
24 % Array initialization with first helix
25
26 Xoffset_start = Xoffset;
27 Yoffset_start = Yoffset;
28
29 path = [-999 -999 -999; -999 -999 -999];
30 path = [path ; helix_down(turns,pitch,radius,ppt, ...
       Xoffset,Yoffset)];
31 path = [path ; [-999 -999 -999; -999 -999 -999]];
32
33 % Loop for array writing in the piezo range
34 while (1)
35     while (1)
36         Xoffset = Xoffset+AddXoffset;
```

```matlab
37              if (Xoffset>(300+radius-Xoffset_start))
38                  break
39              end
40              path = [path ; helix_down(turns,pitch,radius,ppt, ...
                    Xoffset,Yoffset)];
41              path = [path ; [-999 -999 -999; -999 -999 -999]];
42          end
43          Xoffset = Xoffset_start;
44          Yoffset = Yoffset+AddYoffset;
45          if (Yoffset>(300+radius-Yoffset_start))
46              break
47          end
48          path = [path ; helix_down(turns,pitch,radius,ppt, ...
                Xoffset,Yoffset)];
49          path = [path ; [-999 -999 -999; -999 -999 -999]];
50  end
51
52  % 3D plot of the array in the piezo range
53  plot3(path(1:end,1), path(1:end,2), path(1:end,3), 'b.')
54  grid on;
55  axis([0 300 0 300 0 50]);
56
57  % Useful information
58  [helix_coordinates,helix_pointdistance] = ...
        helix_down(turns,pitch,radius,ppt,0,0)
59  helix_turnpathlength = helix_pointdistance*ppt
60  maximum_coords = max(path)
61
62  % Storage procedure
63  save('gwldata.mat','path')
64  clear all;
65  load gwldata.mat;
66  save -ascii helix_10x10_t3p6r3ppt30_down.gwl
67
68  %%%%%%%%%%%%%%%%%%%%%%%%%%%%%%%%%%%%%%%%%%%%%%%%%%%%%%%%%%%%%%%%%
```

```matlab
1  function [ path, pointdistance ] = helix_down( turns , pitch ...
       , radius , ppt , Xoffset, Yoffset )
2  % 'helix_down' computes the writing path of a helix
3  % The coordinates are stored in a vector (x,y,z)
4  % Writing direction: From top to bottom (down))
5
6      %   turns          Number of Helix turns
7      %   pitch          Helix pitch[um]
8      %   radius         Helix radius [um]
9      %   ppt            "points per turn" [-]
10     %   Xoffset        Y axis offset
11     %   Yoffset        Y axis offset
12
13     alpha = linspace(0,2*pi,ppt);        % rotation angle
14     x = cos(alpha)*radius+Xoffset;       % x components of one ...
           turn
15     y = sin(alpha)*radius+Yoffset;       % y components of one ...
           turn
16     z = linspace(0,-pitch,ppt);          % z components of Helix
17
18     % Initialization
19     path = [];
20
21     % Compute coordinates for the helix
22     for m = 0:turns-1
23         path = [path ; [x(1:(ppt-1)); y(1:(ppt-1)); ...
               (z(1:(ppt-1))-m*pitch)]'];
24     end
25     path = [path ; [x(1),y(1),z(1)-turns*pitch]];
26
27     % Shift coordiantes to positive values
28     path(1:end,3) = path(1:end,3)+turns*pitch;
29
30     % Useful information
31     pointdistance = sqrt((path(end,1)-path(end-1,1))^2 ...
32                     +(path(end,2)-path(end-1,2))^2 ...
33                     +(path(end,3)-path(end-1,3))^2);
34
35  end
```

For the writing of bacteria-like structures, the function (used in the helix array assembler code) was replaced: Additionally to the helical flagella a head section was added.

```matlab
function [ path , pointdistance ] = bacteria_down( turns , ...
    pitch , radius , ppt , Xoffset, Yoffset)
% 'bacteria_down' computes the writing path of a bacteria
% The coordinates are stored in a vector (x,y,z)
% Writing direction: From top to bottom (down)

    %   turns          Number of Helix turns
    %   pitch          Helix pitch[um]
    %   radius         Helix radius [um]
    %   ppt            "points per turn" [-]
    %   Xoffset        Y axis offset
    %   Yoffset        Y axis offset

    alpha = linspace(0,2*pi,ppt);    % rotation angle
    x = cos(alpha)*radius+Xoffset;   % x components of a helix ...
        turn
    y = sin(alpha)*radius+Yoffset;   % y components of a helix ...
        turn
    z = linspace(0,-pitch,ppt);      % z components of Helix

    % Initialization
    path = [];

    % Compute coordinates for the bacteria head
    head_turns = pitch*3;
    head_pitch = 0.5;
    z_head = linspace(head_turns*head_pitch, ...
            head_turns*head_pitch-head_pitch,ppt);

    for m = 0:head_turns-1
        path = [path ; [x(1:(ppt-1)); y(1:(ppt-1)); ...
            (z_head(1:(ppt-1))-m*head_pitch)]'];
    end

    % Compute coordinates for the bacteria flagella
    for m = 0:turns-1
```

```matlab
33          path = [path ; [x(1:(ppt-1)); y(1:(ppt-1)); ...
                (z(1:(ppt-1))-m*pitch)]'];
34      end
35      path = [path ; [x(1),y(1),z(1)-turns*pitch]];
36
37      % Shift coordiantes to positive values
38      path(1:end,3) = path(1:end,3)+turns*pitch;
39
40      % Useful information
41      pointdistance = sqrt((path(end,1)-path(end-1,1))^2 ...
42                      +(path(end,2)-path(end-1,2))^2 ...
43                      +(path(end,3)-path(end-1,3))^2);
44  end
```

B.2   DeScribe Programming (gwl-code)

In DeScribe, a programming tool for the general writing language (gwl) provided by Nanoscribe GmbH, there were no commands provided for loops. Therefore it was just used for the final handling of the previously generated structure arrays (by MATLAB) in terms of writing parameter definitions and motorized stage movement commands. The following scripts have been dived into several sub-codes for a better overview. In the same way the MATLAB generated gwl-file is included, all gwl files are combined in a final header gwl-file.

```
1  %%%%%%%%%%%%%%%%%%%%%%%%%%%%%%%%%%%%%%%%%%%%%%%%%%%%%%%%%%%%%
2  %%%%%%%%%%%%%          Helix100_tilt5.gwl          %%%%%%%%%%%%%
3  %%%%%%%%%%%%%%%%%%%%%%%%%%%%%%%%%%%%%%%%%%%%%%%%%%%%%%%%%%%%%
4
5  MoveStageX 150
6  MoveStageY 150
7  MeasureTilt 5          % Tilt measured in 5x5 points
8  MoveStageX −150
9  MoveStageY −150
10
11 include helix_10x10_t3p6r3ppt30_down.gwl  %(MATLAB generated)
12
13 %%%%%%%%%%%%%%%%%%%%%%%%%%%%%%%%%%%%%%%%%%%%%%%%%%%%%%%%%%%%%
```

```
1  %%%%%%%%%%%%%%%%%%%%%%%%%%%%%%%%%%%%%%%%%%%%%%%%%%%%%%%%%%%%%%
2  %%%%%%%%%%%%%             Helix500r3.gwl          %%%%%%%%%%%%
3  %%%%%%%%%%%%%%%%%%%%%%%%%%%%%%%%%%%%%%%%%%%%%%%%%%%%%%%%%%%%%%
4
5  %%%%%%%%%%%%%%%%%%%%%%%%%%%%%%%%%%%%%%%%%%%%%%%%%%%%%%%%%%%%%%
6  %%%%%%%%%%%%%             Initialization          %%%%%%%%%%%%
7
8  PowerScaling 1.00   % PowerScaling (Set absolute power ...
       scaling (0.00 − 1.00); 0.00 = no power; 1.00 = full power)
9  PerfectShape 0      % This PerfectShape feature allows for ...
       avoiding roundish corners even at high writing speeds.
10 Monitoring 0        % Monitoring (Log effective positions; 0 ...
       = off [default]; 1 = on)
11 OperationMode 1     % OperationMode (Mode of Operation; 0 = ...
       pulsed mode; 1 = continuous mode; 2 = fast mode with ...
       logging of effective positions)
12
13 ConnectPoints 1
14 Pointdistance 50
15 ScanSpeed 50
16 Laserpower 10
17
18 %%%%%%%%%%%%%%%%%%%%%%%%%%%%%%%%%%%%%%%%%%%%%%%%%%%%%%%%%%%%%%
19 %%%%%%%%%%%%%             Write structures        %%%%%%%%%%%%
20
21 MoveStageX −1000
22 include Helix100_tilt5.gwl
23 MoveStageX 500
24 include Helix100_tilt5.gwl
25 MoveStageX 500
26 include Helix100_tilt5.gwl
27 MoveStageX 500
28 include Helix100_tilt5.gwl
29 MoveStageX 500
30 include Helix100_tilt5.gwl
31
32 %%%%%%%%%%%%%%%%%%%%%%%%%%%%%%%%%%%%%%%%%%%%%%%%%%%%%%%%%%%%%%
```

```
1   %%%%%%%%%%%%%%%%%%%%%%%%%%%%%%%%%%%%%%%%%%%%%%%%%%%%%%%%%%%%%
2   %%%%%%%    MULTISAMPLE_Helix1500r3_Bacteria500r3    %%%%%%%
3   %%%%%%%%%%%%%%%%%%%%%%%%%%%%%%%%%%%%%%%%%%%%%%%%%%%%%%%%%%%%%
4   %                                                         %
5   %            For 30 mm diameter sample holder:            %
6   %                                                         %
7   %                 1       2       3                       %
8   %            (4)      5       6      (7)                  %
9   %                 8       9       10                      %
10  %                                             TOP         %
11  %%%%%%%%%%%%%%%%%%%%%%%%%%%%%%%%%%%%%%%%%%%%%%%%%%%%%%%%%%%%%
12
13  % Position 4 and 7 do not provide camera view!
14  % If the AZ9260 photo resist thickness is below 20 um:
15  % Interfaceposition = PRthickness + SubstrateAnchorDepth
16  % For ITO coated samples:
17  % Don't forget to set the 'minimal amplitude' to 250 !
18
19  timestamp 1
20
21  Interfaceposition 20
22
23  MessageOut Approach Sample at Position 5
24  SamplePosition 5
25  CenterStage
26  Include Helix500r3.gwl
27  MoveStageX −1000
28  MoveStageY −1000
29  Include Helix500r3.gwl
30  MoveStageX −1000
31  MoveStageY −1000
32  Include Helix500r3.gwl
33
34  MessageOut Approach Sample at Position 6
35  SamplePosition 6
36  CenterStage
37  MoveStageY 1000
38  Include Bacteria500r3.gwl
39
40  %%%%%%%%%%%%%%%%%%%%%%%%%%%%%%%%%%%%%%%%%%%%%%%%%%%%%%%%%%%%%
```

The presented multi-level programming is recommended for large scripts. For practical purposes some of the subcodes were combined into a single gwl-file. All files used in this project and can be found on the DVD. An index of the DVD content can be found in Appendix C.

C   Files on DVD

Data/	Analysis/		EDX/
			VSM (Fe)
	Images/		LM/
			SEM/
			FIB/
	Programming/		CAD/
			MATLAB/
			gwl/
	Videos/		CoNi/
			Fe/
			CoNiAu/
	Workflow Protocol.xlsx		

Thesis/	Presentation/
	Report LaTeX/
	Ferromagnetic Artificial Bacterial Flagella.pdf